IEEE Access
Multidisciplinary ⋮ Rapid Review ⋮ Open Access Journal

Received 13 April 2023, accepted 9 June 2023, date of publication 14 June 2023, date of current version 12 July 2023.

Digital Object Identifier 10.1109/ACCESS.2023.3286015

RESEARCH ARTICLE

Synchronization of Chaotic RCL Shunted-Josephson Junction Systems With Unknown Parametric Uncertainties: Applications to Secure Communication Systems

MUHAMMAD SHAFIQ[1], (Senior Member, IEEE), ISRAR AHMAD[2], AND BASHIR NADERI[3]
[1]Department of Electrical and Computer Engineering, Sultan Qaboos University, Muscat 123, Oman
[2]Department of General Requirements, College of Applied Sciences Nizwa, University of Technology and Applied Sciences, Muscat 611, Oman
[3]Department of Mathematics, Payame Noor University (PNU), Tehran 19395-4697, Iran

Corresponding author: Israr Ahmad (iak_2000plus@yahoo.com)

ABSTRACT The RCL Shunted-Josephson Junction (RCLSJJ) circuit models are complex. They show chaotic behaviour due to internal and external perturbations such as environmental noise, high operational frequencies, parameter variations, and external device forces. The RCLSJJ chaotic behaviour has applications in secure information communication systems (SICS). SICS require synchronization to recover the original signals. This research article proposes a novel adaptive robust control strategy for synchronizing two identical RCLSJJ chaotic systems exposed to bounded unknown exogenous disturbances and un-modelled dynamics. The proposed control strategy achieves faster and smoother convergence of the synchronization error vector to zero. This controller synthesis the control signals without eliminating the nonlinear terms in the closed-loop and is independent of the system's parameters. These characteristics make the closed-loop performance robust, ensuring smooth state-variable trajectories. The proposed controller uses estimates of unknown model uncertainties and bounds to compensate for unknown exogenous disturbances. Proofs of mathematical analysis are based on the Lyapunov second theorem of stability. Theoretical findings get verified through computer simulations showing that the proposed control technique quickly compels the error vector to the origin with less active oscillations for all signals. Comparative computer simulations confirm that the performance of the designed controller is better than the other state-of-the-art feedback controllers. The proposed strategy is applied to encrypt and decrypt one-dimensional and two-dimensional messages in secure communication systems.

INDEX TERMS Adaptive controller, RCL shunted-Josephson junction model, chaos synchronization, Lyapunov stability theory, secure communications.

I. INTRODUCTION

In natural and social sciences, some dynamical systems exhibit chaos, which results in irregular and unpredictable complex signals due to their aperiodicity and limited predictability [1]. Chaotic systems are characterized by strange attractors with fractal or multi-fractal structures [2], defying synchronization behaviour. Two or more chaotic systems can synchronize with a strong coupling force, oscillating in the same response time [3]. The synchronization phenomenon has significant applications in various fields such as aeronautical and space engineering, electronics, power grids, robotics, biophysical and mechanical systems [4], [5], [6], [7], [8], [9] (among others). For example, chaotic gyroscope synchronization performs navigations and provides stability in orbiting satellites, automobiles, and space launch vehicles [4]. Spontaneous synchronization in power grids is desirable to ensure that introducing alternative power sources, i.e. solar, wind, and other sources, does not disturb its synchronization attitude [5]. Chaos synchronization

The associate editor coordinating the review of this manuscript and approving it for publication was Zheng Chen.

compensates for load disturbances in the single-machine infinite bus, facilitating an interference-free electric power supply [6]. Synchronization in the coronary artery system helps diagnose cardiopathy risk and propose treatment to prevent arrhythmia problems [7].

Various feedback control strategies have been developed to synchronize chaotic systems, including sliding mode control [10], nonlinear control technique [11], sample data control method [12], adaptive control methodology [13], H_∞ control design approach [14], etc. Among these, the adaptive control technique is an effective strategy for controlling slow time-varying dynamical systems.

The Josephson Junction devices show high operating frequency and low energy consumption [15]. Various Josephson Junction models, including the RCL Shunted-Josephson Junction (RCLSJJ), are reported in the literature [16], [17], [18]. Despite their irregular complex behaviour [19], RCLSJJs can maintain a stable frequency for an extended period, making them useful for applications that require precise timing, amplitude, and frequency [20]. These include superconducting quantum interference devices (SQUIDs), superconducting qubits, high-frequency signal generators, superconducting resonators, and sensors for various applications [21], [22]. The RCLSJJs' circuit parameters can vary due to internal and external factors, producing resonance perturbations and generating chaos in the system [16]. The RCLSJJ model is primarily used to study superconducting Josephson junctions' dynamics under an external electromagnetic field [17]. It is also used to construct the Bloch oscillating transistor [23].

The RCLSJJ chaotic systems' synchronization has potential applications in different fields. Using synchronized Josephson junctions in high-temperature superconductors makes it possible to construct a compact Terahertz oscillator [24]. Although a single Josephson junction's radiation is weak, power radiation from synchronized Josephson junctions is feasible [25]. Two chaotic RCLSJJ models can form encryption and decryption of messages in secure communication systems using synchronization arrangements [26]. Several feedback controller schemes synchronizing coupled chaotic RCLSJJ systems' behaviour are available in the literature. A brief review of this research is as follows.

Ucar et al. [27] proposes an active control methodology investigating the synchronization of two coupled chaotic RCLSJJ systems. The closed-loop stability is investigated using the Routh-Hurwitz criterion, assuming that the state variables are measurable and parameters are known prior. Vincent et al. [28] utilizes a Lyapunov-based backstepping feedback control design to accomplish chaos control and synchronization of the RCLSJJ chaotic system. Motivated to reduce the number of control inputs, Chen et al. [29] develops a single input sliding mode controller that realizes two identical chaotic RCLSJJ systems synchronization with noise disturbances. The adaptive control strategy [30] accomplishes uncertain RCLSJJ chaotic systems synchronization. Ojo et al. [31] uses the active backstepping control design to achieve three chaotic RCLSJJ systems compound synchronization. Khooshehmehri et al. [32] recently developed a robust adaptive controller synchronizing two coupled chaotic RCLSJJ systems with un-modelled dynamics.

The following items discuss the motivations and challenges.

1) The articles [27], [28], [29], [30], [31], [32] propose feedback control strategies to synchronize two identical chaotic RCLSJJ systems using the nonlinear terms cancellation approach. These approaches require the exact measurement of state variables and parameters, which is impossible technologically. Even precise measurement processes are complicated due to noise and parameter uncertainties in the measurement system and plant dynamics [13]. Consequently, employing such control design strategies [27], [28], [29], [30], [31], [32] leads to residual nonlinear parts in the closed-loop system, leading to erroneous control efforts and causing instability [13]. These residual terms generally affect closed-loop performance, including transient behaviour and steady-state, leading to long-time delays.
2) The feedback controller approaches [27], [28], [29], [30], [31], [32] develop control signals that produce large oscillations generating voltage fluctuations in the RCLSJJ system. These fluctuations affect the smooth, steady flow of current, which cause adverse effects on the synchronization performance. As a consequence, the closed-loop system may become unstable.
3) External sources, such as current flow and voltage fluctuations, can generate disturbances in RCLSJJ circuits, which can negatively impact their performance due to conduction, electrostatic coupling, or electromagnetic induction [33]. The noisy environment and fluctuations due to high operational frequencies cause uncertainties in the RCLSJJ circuit's parameters [22], [23], [24], affecting the proposed control design methodologies [27], [28], [29], [30], [31], [32]. As a result, the closed-loop system may lose its stability.
4) Reducing energy consumption in the synchronization process is a challenging problem. Fluctuation-free error convergence consumes low energy, inspiring the development of fast convergence synchronization controllers with lesser oscillations [13]. The accuracy of synchronizing coupled RCLSJJ chaotic systems maintains the smooth flow of current and retains the standard voltage [33]. The feedback controller approaches [27], [28], [29], [30], [31], [32] require hefty controller gains to reduce fluctuations in the synchronization error signals. However, significant amplitude control signals oscillation still exists. This controller's attribute demands high energy. Moreover, heightened gains lead to overshooting the system's state variables and saturation of the controller's output, which may render the closed-loop system unstable.

5) In practice, fast convergence rates are desirable to ensure optimal system performance in a rapidly changing environment. Slow convergence rates may cause the actuator to malfunction, and the system performs poorly. The feedback controllers [27], [28], [29], [30], [31], [32] offer a smaller synchronization error convergence gradient, resulting in slow error convergence behaviour.

The above challenges motivate designing state-feedback controllers for synchronizing two identical RCLSJJ chaotic systems possessing the following attributes.

1) The controller should avoid the closed-loop's nonlinear terms cancellation.
2) It should be robust to time-varying unknown model uncertainties and exogenous disturbances and accomplish faster error vector convergence rates.
3) It should generate error and control signals with reduced oscillations.

This article aims to achieve the following two main objectives regarding controller design.

1) Robust closed-loop development
   The closed-loop state variables should be insensitive to the exogenous disturbances and smooth slow parameter variations, i.e. the synthesized control effort should penalize these effects.
2) Synthesizing a smooth control effort
   The controller should synthesize a smooth control effort for an energy-efficient closed loop that maintains chaotic RCLSJJ systems synchronization stability, ensuring steady current and voltage flow without inducing closed-loop dynamics fluctuations.

Therefore, this article proposes a novel robust direct adaptive synchronization control strategy (RDASCS) that resolves the above challenges. The article discusses closed-loop stability based on mathematical analysis, computer simulations, and comparative theoretical and analytical critique.

The analysis shows that the proposed RDASCS attributes are as follows.

1) The developed closed-loop is robust-stable, oscillation free, and fast.
2) The control law does not rely on cancelling the closed-loop dynamical system's nonlinear terms; therefore, the closed loop is irresponsive to time-varying exogenous disturbances and model uncertainties.
3) The control signals are smooth; such control efforts do not develop oscillations in the system dynamics and keep the closed-loop robust-stable.

The paper proves the closed-loop robust asymptotic stability using the Lyapunov second theorem of stability [34]. The closed-loop performance is compared with other recently state-of-the-art synchronization control methods [32], [35] discussing the synchronization of similar chaoticsystems. The proposed algorithm is also applied to secure communication systems for encrypting and decrypting one-dimensional and two-dimensional messages.

The rest of the paper is organized as follows.

Section II describes the terminology. In Section III, the article illustrates the RCLSJJ system's chaotic dynamics. Section IV formulates the problem of synchronizing two identical RCLSJJ chaotic systems. Section V designs a novel adaptive feedback controller for synchronizing master-slave RCLSJJ chaotic systems and proves robust closed-loop stability. Section VI gives numerical simulations with comparative studies and applications to SCS. Section VII concludes the manuscript.

II. NOTATIONS AND SYMBOLS

Table 1 describes the terminology.

III. THE CHAOTIC RCL SHUNTED-JOSEPHSON JUNCTION CIRCUIT DYNAMICS

Equation (1) represents the normalized form of the RCLSJJ system [16].

$$\begin{aligned} \frac{h}{2q_e}\frac{d\theta(t)}{dt} &= V(t) \\ C\frac{dV(t)}{dt} + \frac{V(t)}{R_V} + I_c\sin\theta(t) + I_s(t) &= I \\ V(t) = L_s\frac{dI_s(t)}{dt} + I_s(t)R_s & \end{aligned} \tag{1}$$

where q_e represents the electronic charge, and h is the plank constant. $V(t)$, L_s, and R_s are the Josephson junction voltage, shunt inductance, and shunt resistance, alternatively. $\theta(t)$, I, and $I_s(t)$ denote the superconducting order parameter phase difference across the junction, input DC bias, and shunt current, alternatively. R_V, I_c, and C indicate the nonlinear junction resistance, critical current, and capacitance alternatively.

The nonlinear junction resistance R_V is described in (2).

$$R_V = \begin{cases} R_N, & |V| > V_g \\ R_{sg}, & |V| \le V_g \end{cases} \tag{2}$$

where $V_g = \frac{2\Delta}{q_e}$ denotes the gap voltage that depends on the Josephson junction energy gap Δ. R_{sg} and R_N represent the sub-gap resistance and normal state resistance, respectively.

Let $x_1(t) = \theta(t)$, $x_2(t) = V(t)$, and $x_3(t) = I_s(t)$, Eq. (3) represents the RCLSJJ system dynamics in state-space format.

$$\begin{aligned} \dot{x}_1(t) &= x_2(t) \\ \dot{x}_2(t) &= -\frac{1}{\beta_c}gx_2(t) - \frac{1}{\beta_c}(x_3(t) + \sin x_1(t) - i) \\ \dot{x}_3(t) &= -\frac{1}{\beta_L}x_3(t) + \frac{1}{\beta_L}x_2(t) \end{aligned} \tag{3}$$

where $\beta_c = \frac{4\pi I_c R_s^2 C}{h}$, $\beta_L = \frac{4\pi e I_c L}{h}$, and $g = \frac{R_s}{R_V}$. β_c, β_L, and i denote the capacitance, inductance, and external current, alternatively [16], [18]. For numerical simulations, let us choose $\beta_c = 0.707$, $\beta_L = 2.68$, $g = 0.0478$, and $i = 1.2$ [16], [18]. Equation (4) describes the RCLSJJ chaotic

TABLE 1. Notations and symbols.

Symbols	Description
$\mathbf{x}$ and $\mathbf{X}$	$\mathbf{x}$ denotes an $n \times 1$ vector, and $\mathbf{X}$ represents an $n \times n$ matrix
R	Real numbers
$(\varphi_1, \varphi_2) \in R$	An open interval between φ_1 and φ_2
T	Vector/Matrix transpose
MSS	Master-Slave system
$\mathbf{x}(t) = [x_1(t) \quad x_2(t) \quad \ldots \quad x_n(t)]^T \in R^{n\times 1}$	Vector of the state variables
$\mathbf{x}(t) = [x_1(t) \quad x_2(t) \quad x_3(t)]^T \in R^{n\times 1}$	RCLSJJ chaotic systems' (4) state variables vector
a_1, a_2, a_3, and a_4	RCLSJJ chaotic systems' (4) constant parameters
$\mathbf{x}^m(t) = [x_1^m(t) \quad x_2^m(t) \quad x_3^m(t)]^T \in R^{3\times 1}$, and $\mathbf{x}^s(t) = [x_1^s(t) \quad x_2^s(t) \quad x_3^s(t)]^T \in R^{3\times 1}$	Master and slave systems (5-6) state variables vectors
$\mathbf{e}(t) = \mathbf{x}^s(t) - \mathbf{x}^m(t) = [e_1(t) \quad e_2(t) \quad e_3(t)]^T \in R^{3\times 1}$	Synchronization error vector
$\boldsymbol{\phi}^m(\mathbf{x}^m(t)) = \{\phi_{ij}^m(x_i^m(t)), i \neq j \Rightarrow \phi_{ij}^m(x_i^m(t)) = 0\} \in R^{3\times 3}$, and $\boldsymbol{\phi}^s(\mathbf{x}^s(t)) = \{\phi_{ij}^s(x_i^s(t)), i \neq j \Rightarrow \phi_{ij}^s(x_i^s(t)) = 0\} \in R^{3\times 3}$, $i,j = 1,2,3$	Unknown time-varying model uncertainties present in the MSS (5-6), respectively
$\boldsymbol{\phi}^m = \{\phi_{ij}^m, i \neq j \Rightarrow \phi_{ij}^m = 0\} \in R^{3\times 3}$, $\boldsymbol{\phi}^s = \{\phi_{ij}^s, \ i \neq j \Rightarrow \phi_{ij}^s = 0,\} \in R^{3\times 3}$, and $\boldsymbol{\phi}^m + \boldsymbol{\phi}^s = \boldsymbol{\phi} = \{\phi_{ij}, \quad i \neq j \Rightarrow \phi_{ij} = 0,\} \in R^{3\times 3}$, $i,j = 1,2,3$	$\boldsymbol{\phi}^m$ and $\boldsymbol{\phi}^s$ are the matrices that represent the least upper bounds of $\boldsymbol{\phi}^m(\mathbf{x}^m(t))$ and $\boldsymbol{\phi}^s(\mathbf{x}^s(t))$, respectively
$\boldsymbol{\phi}_D^m(\mathbf{x}^m(t)) = \{\phi_{Ci}^m(x_i^m(t)) = \phi_{ii}^m(x_i^m(t))\} \in R^{3\times 1}$, $\boldsymbol{\phi}_D^s(\mathbf{x}^s(t)) = \{\phi_{Ci}^s(x_i^m(t)) = \phi_{ii}^s(x_i^s(t))\} \in R^{3\times 1}$, $\boldsymbol{\phi}_D^m = \{\phi_{Ci}^m = \phi_{ii}^m\} \in R^{3\times 1}$, and $\boldsymbol{\phi}_D^s = \{\phi_{Ci}^s = \phi_{ii}^s\} \in R^{3\times 1}$, $i,j = 1,2,3$	$\boldsymbol{\phi}_D^m(\mathbf{x}^m(t))$, $\boldsymbol{\phi}_D^s(\mathbf{x}^s(t))$, $\boldsymbol{\phi}_D^m$, and $\boldsymbol{\phi}_D^s$ are column vectors containing the diagonal elements of $\boldsymbol{\phi}^m(\mathbf{x}^m(t))$, $\boldsymbol{\phi}^s(\mathbf{x}^s(t))$, $\boldsymbol{\phi}^m$, and $\boldsymbol{\phi}^s$, alternatively
$\boldsymbol{\Gamma}^m(t) = \{\gamma_{ij}^m(t), \ i \neq j \Rightarrow \gamma_{ij}^m(t) = 0\} \in R^{3\times 3}$, and $\boldsymbol{\Gamma}^s(t) = \{\gamma_{ij}^s(t), i \neq j \Rightarrow \gamma_{ij}^s(t) = 0\} \in R^{3\times 3}$, $i,j = 1,2,3$	Unknown time-varying exogenous disturbances acting on the MSS (5-6), respectively
$\boldsymbol{\Gamma}^m = \{\gamma_{ij}^m, i \neq j \Rightarrow \gamma_{ij}^m = 0\} \in R^{3\times 3}$, $\boldsymbol{\Gamma}^s = \{\gamma_{ij}^s, i \neq j \Rightarrow \gamma_{ij}^s = 0\} \in R^{3\times 3}$, and $\boldsymbol{\Gamma}^m + \boldsymbol{\Gamma}^s = \boldsymbol{\Gamma} = \{\gamma_{ij}, \ i \neq j \Rightarrow \gamma_{ij} = 0,\} \in R^{3\times 3}$, $i,j = 1,2,3$	$\boldsymbol{\Gamma}^m$ and $\boldsymbol{\Gamma}^s$ are the matrices that represent the least upper bounds of $\boldsymbol{\Gamma}^m(t)$ and $\boldsymbol{\Gamma}^s(t)$, respectively
$\boldsymbol{\Gamma}_D^m(t) = \{\gamma_{Ci}^m(t) = \gamma_{ii}^m(t)\} \in R^{3\times 1}$, $\boldsymbol{\Gamma}_D^s(t) = \{\gamma_{Ci}^s(t) = \gamma_{ii}^s(t)\} \in R^{3\times 1}$, $\boldsymbol{\Gamma}_D^m = \{\gamma_{Ci}^m = \gamma_{ii}^m\} \in R^{3\times 1}$, and $\boldsymbol{\Gamma}_D^s = \{\gamma_{Ci}^s = \gamma_{ii}^s\} \in R^{3\times 1}$, $i,j = 1,2,3$	$\boldsymbol{\Gamma}_D^m(t)$, $\boldsymbol{\Gamma}_D^s(t)$, $\boldsymbol{\Gamma}_D^m$, and $\boldsymbol{\Gamma}_D^s$ are column vectors containing the diagonal elements of $\boldsymbol{\Gamma}^m(t)$, $\boldsymbol{\Gamma}^s(t)$, $\boldsymbol{\Gamma}^m$, and $\boldsymbol{\Gamma}^s$, alternatively
$\mathbf{u}(t) = [u_1(t) \quad u_2(t) \quad u_3(t)]^T \in R^{3\times 1}$	Vector of the control input
$\varphi, \sigma, \eta_{ii}, i = 1,2,3$	Controller parameters
ϱ, ρ	Real constants
e	Logarithmic base
$\mathbf{A} = \{\alpha_{ij}, i \neq j \Rightarrow \alpha_{ij} = 0\} \in R^{3\times 3}$, $\mathbf{B}(t) = \{\beta_{ij}(t), i \neq j \Rightarrow \beta_{ij}(t) = 0\} \in R^{3\times 3}$, and $\beta_{ii}(t) = \eta_{ii}(1 - \rho e^{-\varrho \lvert e_i(t) \rvert})$, $i,j = 1,2,3$	The feedback controller gains matrices
$\hat{\boldsymbol{\Phi}}(t) = \{\hat{\phi}_{ij}(t), \ i \neq j \Rightarrow \hat{\phi}_{ij}(t) = 0\} \in R^{3\times 3}$, and $\hat{\boldsymbol{\Gamma}}(t) = \{\hat{\gamma}_{ij}(t), i \neq j \Rightarrow \gamma_{ij}(t) = 0\} \in R^{3\times 3}$, $i,j = 1,2,3$	Parameters of the controller (14), which are unknown
$\hat{\boldsymbol{\Phi}}_D(t) = \{\hat{\phi}_{ci}(t) = \hat{\phi}_{ii}(t)\} \in R^{3\times 1}$, and $\hat{\boldsymbol{\Gamma}}_D(t) = \{\hat{\gamma}_{Ci}(t) = \hat{\gamma}_{ii}(t)\} \in R^{3\times 1}$, $i,j = 1,2,3$	$\hat{\boldsymbol{\Phi}}_D(t)$ and $\hat{\boldsymbol{\Gamma}}_D(t)$ are column vectors containing the diagonal elements of $\hat{\boldsymbol{\Phi}}(t)$, and $\hat{\boldsymbol{\Gamma}}(t)$, respectively
$\dot{V}(\mathbf{e}(t))$	The time derivative of $V(\mathbf{e}(t))$
$\lvert x \rvert$	Absolute of a scalar, where $x \in R$
$\lvert \mathbf{x} \rvert = [\lvert x_1 \rvert, \lvert x_2 \rvert, \lvert x_3 \rvert]^T$	Absolute of a vector, where $\mathbf{x} \in R^{3\times 1}$ and $x_i \in \mathbf{x}$, $i = 1,2,3$
$\lVert \mathbf{x} \rVert = \sum_1^3 \lvert x_i \rvert$	Norm-1 of $\mathbf{x}$
$\lvert \mathbf{X} \rvert = \{\lvert X_{ij} \rvert, i,j = 1,2,3\} \in R^{3\times 3}$, where $X_{ij} \in R$	Absolute of a matrix

system (3) matrix form.

$$\dot{\mathbf{x}}(t) = \begin{bmatrix} \dot{x}_1(t) \\ \dot{x}_2(t) \\ \dot{x}_3(t) \end{bmatrix} = \begin{bmatrix} 0 & 1 & 0 \\ 0 & -a_1 a_3 & -a_1 \\ 0 & a_2 & -a_2 \end{bmatrix} \begin{bmatrix} x_1(t) \\ x_2(t) \\ x_3(t) \end{bmatrix} + \begin{bmatrix} 0 \\ -a_1 \sin x_1(t) \\ 0 \end{bmatrix} + \begin{bmatrix} 0 \\ a_1 a_4 \\ 0 \end{bmatrix}, \quad (4)$$

where $a_1 = \frac{1}{\beta_c}$, $a_2 = \frac{1}{\beta_L}$, $a_3 = g$, and $a_4 = i$.

Figure 1 shows the RCL-Shunted-Josephson Junction circuit diagram. The RCLSJJ circuit system exhibits chaos for the values of the parameters $a_1 = 1.4144$, $a_2 = 0.3731$, $a_3 = 0.0478$, and $a_4 = 1.2$. Figures 2, 3(a-c) and 4(a-c) depict the 3D chaotic attractor, bifurcation diagrams, and Poincare maps, alternatively. For the 2D chaotic attractor and state variable trajectories' chaotic behaviour, one may refer to [16] and [18]. The computer simulation results in this article consider initial conditions $x_1(t) = 0.1$, $x_2(t) = 0.2$, and $x_3(t) = 0.3$.

IV. PROBLEM STATEMENT

This section describes the MSS synchronization model for the RCLSJJ system (4) and defines the MSS error dynamics.

A. SYNCHRONIZATION MODEL FOR TWO IDENTICAL RCLSJJ CHAOTIC SYSTEMS

Equations (5-6) describe the MSS synchronization model for two identical chaotic RCLSJJ systems. Let $\dot{\mathbf{x}}^m(t)$ represents the master chaotic RCLSJJ system (5) and $\dot{\mathbf{x}}^s(t)$ the slave chaotic RCLSJJ system (6). Further, $\boldsymbol{\Gamma}^m(t)$ and $\boldsymbol{\Gamma}^s(t)$ denote unknown time-varying bounded exogenous disturbances acting on the MSS (5-6), respectively and $\boldsymbol{\phi}^m(\mathbf{x}^m(t))$ and $\boldsymbol{\phi}^s(\mathbf{x}^s(t))$ are unknown bounded model uncertainties present in the MSS (5-6), respectively. $\mathbf{u}(t) \in R^{3\times 1}$ is the control input vector applied to the slave chaotic RCLSJJ system (6).

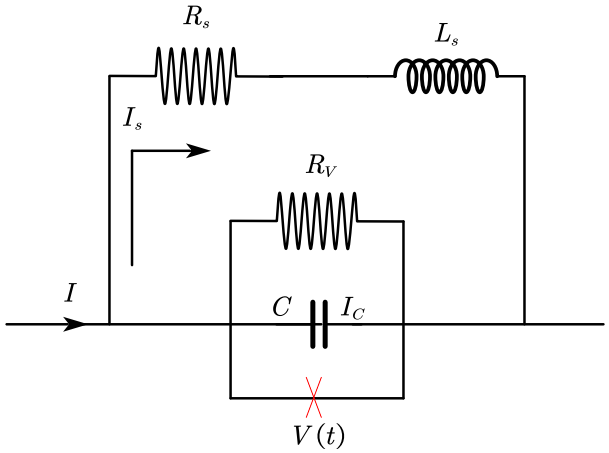

FIGURE 1. RCL-Shunted-Josephson Junction circuit diagram.

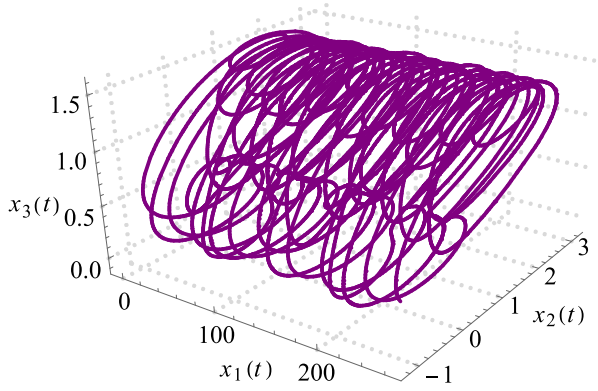

FIGURE 2. 3D phase portrait.

Many articles consider such uncertainties as a function of state variables [36], [37].

(Master chaotic RCLSJJ system)

$$\dot{\mathbf{x}}^m(t) = \begin{bmatrix} \dot{x}_1^m(t) \\ \dot{x}_2^m(t) \\ \dot{x}_3^m(t) \end{bmatrix} = \begin{bmatrix} 0 & 1 & 0 \\ 0 & -a_1a_3 & -a_1 \\ 0 & a_2 & -a_2 \end{bmatrix} \begin{bmatrix} x_1^m(t) \\ x_2^m(t) \\ x_3^m(t) \end{bmatrix} + \begin{bmatrix} 0 \\ -a_1 \sin x_1^m(t) \\ 0 \end{bmatrix} + \begin{bmatrix} 0 \\ a_1a_4 \\ 0 \end{bmatrix} + \boldsymbol{\Phi}^m\left(\mathbf{x}^m(t)\right) + \boldsymbol{\Gamma}^m(t) \tag{5}$$

(Slave chaotic RCLSJJ system)

$$\dot{\mathbf{x}}^s(t) = \begin{bmatrix} \dot{x}_1^s(t) \\ \dot{x}_2^s(t) \\ \dot{x}_3^s(t) \end{bmatrix} = \begin{bmatrix} 0 & 1 & 0 \\ 0 & -a_1a_3 & -a_1 \\ 0 & a_2 & -a_2 \end{bmatrix} \begin{bmatrix} x_1^s(t) \\ x_2^s(t) \\ x_3^s(t) \end{bmatrix} + \begin{bmatrix} 0 \\ -a_1 \sin x_1^s(t) \\ 0 \end{bmatrix} + \begin{bmatrix} 0 \\ a_1a_4 \\ 0 \end{bmatrix} + \boldsymbol{\Phi}^s\left(\mathbf{x}^s(t)\right) + \boldsymbol{\Gamma}^s(t) + \mathbf{u}(t) \tag{6}$$

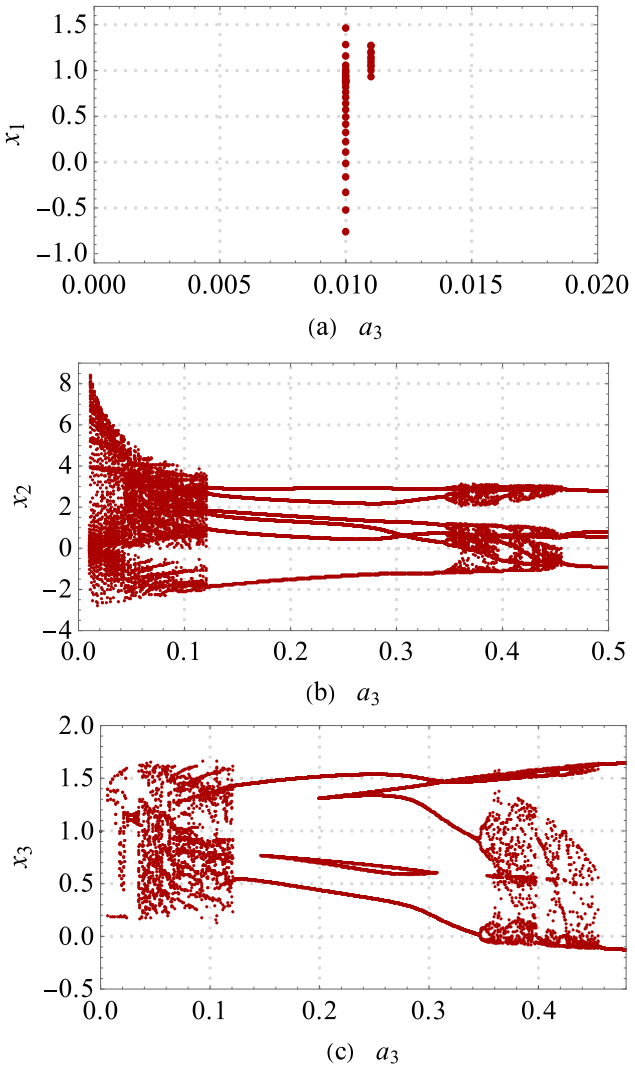

FIGURE 3. Bifurcation diagrams, (a) a_3 vs x_1, (b) a_3 vs x_2, and (c) a_3 vs x_3.

Let $\mathbf{e}(t) = \mathbf{x}^s(t) - \mathbf{x}^m(t)$, then Eq. (7) describes the synchronization error dynamics (5-6).

$$\begin{aligned} \dot{\mathbf{e}}(t) &= \begin{bmatrix} \dot{e}_1(t) \\ \dot{e}_2(t) \\ \dot{e}_3(t) \end{bmatrix} = \begin{bmatrix} 0 & 1 & 0 \\ 0 & -a_1a_3 & -a_1 \\ 0 & a_2 & -a_2 \end{bmatrix} \begin{bmatrix} e_1(t) \\ e_2(t) \\ e_3(t) \end{bmatrix} + \begin{bmatrix} 0 \\ a_1\left(\sin x_1^m(t) - \sin x_1^s(t)\right) \\ 0 \end{bmatrix} + \boldsymbol{\Phi}^s\left(\mathbf{x}^s(t)\right) \\ &\quad - \boldsymbol{\Phi}^m\left(\mathbf{x}^m(t)\right) + \boldsymbol{\Gamma}^s(t) - \boldsymbol{\Gamma}^m(t) + \mathbf{u}(t) \\ &= \begin{bmatrix} 0 & 1 & 0 \\ 0 & -a_1a_3 & -a_1 \\ 0 & a_2 & -a_2 \end{bmatrix} \begin{bmatrix} e_1(t) \\ e_2(t) \\ e_3(t) \end{bmatrix} + \begin{bmatrix} 0 \\ a_1\left(\sin x_1^m(t) - \sin x_1^s(t)\right) \\ 0 \end{bmatrix} \\ &\quad + \boldsymbol{\Phi}^{ms}\left(\mathbf{x}^{ms}(t)\right) + \boldsymbol{\Gamma}^{ms}(t) + \mathbf{u}(t) \end{aligned}$$

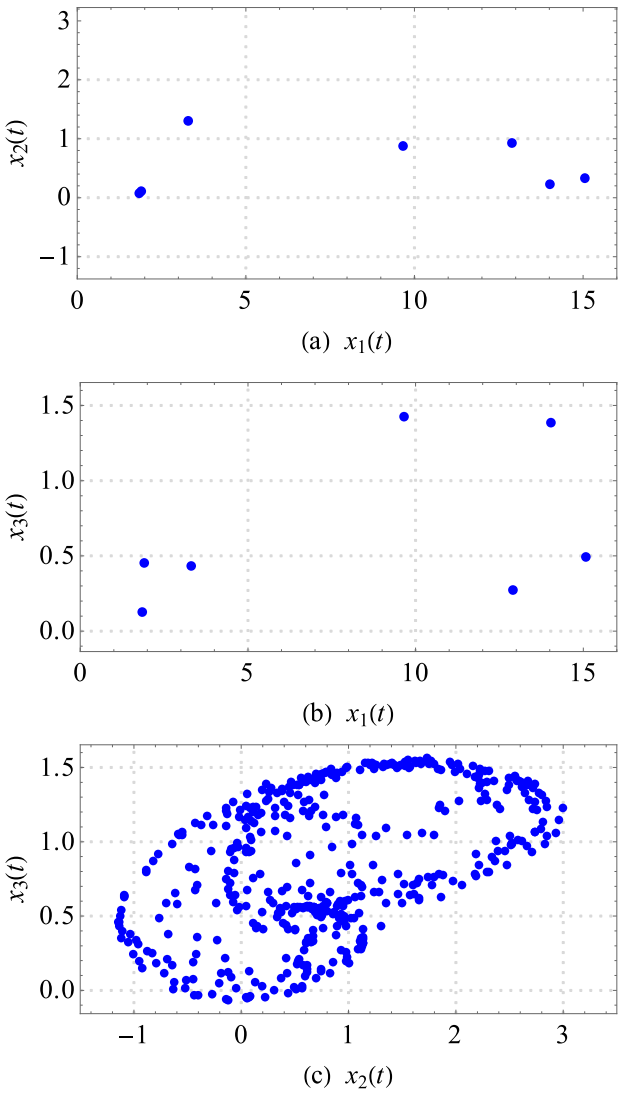

FIGURE 4. Poincare maps, (a) $x_1(t)$ vs $x_2(t)$, (b) $x_1(t)$ vs $x_3(t)$, and (c) $x_2(t)$ vs $x_3(t)$.

$$= \begin{bmatrix} 0 & 1 & 0 \\ 0 & -a_1a_3 & -a_1 \\ 0 & a_2 & -a_2 \end{bmatrix} \begin{bmatrix} e_1(t) \\ e_2(t) \\ e_3(t) \end{bmatrix} + \begin{bmatrix} 0 \\ a_1\left(\sin x_1^m(t) - \sin x_1^s(t)\right) \\ 0 \end{bmatrix} + \boldsymbol{\Psi}^{ms}\left(\boldsymbol{\phi}^{ms}\left(\mathbf{x}^{ms}(t)\right), \boldsymbol{\Gamma}^{ms}(t)\right) + \mathbf{u}(t), \tag{7}$$

where

$$\begin{cases} \boldsymbol{\phi}^{ms}\left(\mathbf{x}^{ms}(t)\right) := \boldsymbol{\phi}^{s}\left(\mathbf{x}^{s}(t)\right) - \boldsymbol{\phi}^{m}\left(\mathbf{x}^{m}(t)\right), \\ \boldsymbol{\Gamma}^{ms}(t) := \boldsymbol{\Gamma}^{s}(t) - \boldsymbol{\Gamma}^{m}(t), \\ \boldsymbol{\Psi}^{ms}\left(\boldsymbol{\phi}^{ms}\left(\mathbf{x}^{ms}(t)\right), \boldsymbol{\Gamma}^{ms}(t)\right) := \boldsymbol{\phi}^{ms}\left(\mathbf{x}^{ms}(t)\right) + \boldsymbol{\Gamma}^{ms}(t). \end{cases}$$

The differential mean-value theorem [38] is used to determine error bounds as a cosine function. By utilizing the Mean-Value theorem,

$$\frac{\sin\varphi_2 - \sin\varphi_1}{\varphi_2 - \varphi_1} = \cos\theta, \tag{8}$$

where $\theta \in (\varphi_1, \varphi_2)$, and $\varphi_1, \varphi_2 \in R$.

Therefore, the expression presented in Eq. (8) can be readily derived.

$$\begin{aligned} \sin x_1^s(t) - \sin x_1^m(t) &= \left(x_1^s(t) - x_1^m(t)\right)\cos\theta(t) \\ &= e_1(t)\cos\theta(t) \end{aligned} \tag{9}$$

Then, using (9) in (7) gives (10).

$$\begin{aligned} \dot{\mathbf{e}}(t) = \begin{bmatrix} \dot{e}_1(t) \\ \dot{e}_2(t) \\ \dot{e}_3(t) \end{bmatrix} &= \begin{bmatrix} 0 & 1 & 0 \\ 0 & -a_1a_3 & -a_1 \\ 0 & a_2 & -a_2 \end{bmatrix} \begin{bmatrix} e_1(t) \\ e_2(t) \\ e_3(t) \end{bmatrix} \\ &- \begin{bmatrix} 0 \\ e_1(t)\cos\theta(t) \\ 0 \end{bmatrix} \\ &+ \boldsymbol{\Psi}^{ms}\left(\boldsymbol{\phi}^{ms}\left(\mathbf{x}^{ms}(t)\right), \boldsymbol{\Gamma}^{ms}(t)\right) + \mathbf{u}(t). \end{aligned} \tag{10}$$

Remark 1: Internal and external disturbances affect the RCLSJJ circuits' performance due to conduction, electrostatic coupling, or electromagnetic induction [33]. In electronic circuits, model uncertainties can arise from various factors, including measurement, dynamic modelling, and control system errors [39], [40]. Rapid variations in the current flow and voltage are the sources of external disturbances in electronic circuits. These disturbances affect the circuits' performance [33]. Further, the random noise sources are mainly due to electronic measurement, thermal noise, shot noise, environmental noise [41], etc. Therefore, it is essential to consider and tackle these disturbances effectively when designing a control algorithm.

Assumption 1: Let us assume the unknown exogenous disturbances $\{\boldsymbol{\Gamma}^m(t), \boldsymbol{\Gamma}^s(t)\}$ and model uncertainties $\left\{\boldsymbol{\phi}^m\left(\mathbf{x}^m(t)\right), \boldsymbol{\phi}^s\left(\mathbf{x}^s(t)\right)\right\}$ are bounded [36], [37], and Eqs. (11a) and (12a) define their bounds, respectively.

$$\left|\gamma_{ii}^m(t)\right| \le \gamma_{ii}^m, \quad \left|\gamma_{ii}^s(t)\right| \le \gamma_{ii}^s, \quad i = 1, 2, 3. \tag{11a}$$

$$\begin{aligned} &\Rightarrow \left|\gamma_{ii}^{ms}(t)\right| = \left|\gamma_{ii}^s(t) - \gamma_{ii}^m(t)\right| \\ &= \left|\gamma_{ii}^s(t) + \left(-\gamma_{ii}^m(t)\right)\right| \\ &\le \left|\gamma_{ii}^s(t)\right| + \left|-\gamma_{ii}^m(t)\right| \\ &\le \left|\gamma_{ii}^s(t)\right| + \left|\gamma_{ii}^m(t)\right| \\ &\le \gamma_{ii}^s + \gamma_{ii}^m \le \gamma_{ii}, \quad i = 1, 2, 3 \end{aligned} \tag{11b}$$

and

$$\left|\phi_{ii}^m\left(x_i^m(t)\right)\right| \le \phi_{ii}^m, \quad \left|\phi_{ii}^m\left(x_i^s(t)\right)\right| \le \phi_{ii}^s, \quad i = 1, 2, 3. \tag{12a}$$

$$\begin{aligned} &\Rightarrow \left|\phi_{ii}^{ms}\left(x_i^{ms}(t)\right)\right| = \left|\phi_{ii}^s\left(x_i^s(t)\right) - \phi_{ii}^m\left(x_i^m(t)\right)\right| \\ &\le \left|\phi_{ii}^s\left(x_i^s(t)\right)\right| + \left|\phi_{ii}^m\left(x_i^m(t)\right)\right| \\ &\le \phi_{ii}^s + \phi_{ii}^m \le \phi_{ii}, \quad i = 1, 2, 3. \end{aligned} \tag{12b}$$

Therefore, from Eqs. (11b) and (12b), it is concluded that:

$$\left|\Psi_{ii}^{ms}\left(\phi_{ii}^{ms}\left(x_i^{ms}(t)\right), \gamma_{ii}^{ms}(t)\right)\right|$$

$$
\begin{aligned}
&= \left|\phi_{ii}^{ms}\left(x_i^{ms}(t)\right) + \gamma_{ii}^{ms}(t)\right| \\
&\leq \left|\phi_{ii}^{ms}\left(x_i^{ms}(t)\right)\right| + \left|\gamma_{ii}^{ms}(t)\right| \\
&\leq \phi_{ii} + \gamma_{ii} = \Psi_{ii}, \quad i = 1, 2, 3, \qquad (13)
\end{aligned}
$$

where $\Psi_{ii} > 0$, $\phi_{ii}^{s} > 0$, $\phi_{ii}^{m} > 0$, $\gamma_{ii}^{s} > 0$, $\gamma_{ii}^{m} > 0$, $\phi_{ii} > 0$, and $\gamma_{ii} > 0$ are unknown real constants. Therefore, $\boldsymbol{\Psi}$ is a diagonal matrix with elements Ψ_{ii}, $i = 1, 2, 3$, representing the combined uncertainties bound.

B. PROBLEMS IN THE CONTROLLERS AND A POSSIBLE SOLUTION

Research articles [27], [28], [29], [30], [31], [32] suggest synthesizing control efforts by designing control laws that eliminate the chaotic RCLSJJ system (4) nonlinear terms. These methodologies need exact state variables and plant parameter measurements, which is technologically impossible. Uncertainties in the measurements cause variation in the voltage, consequently disturbing the current flow smoothness. In general, such limitations produce oscillations in the state variables. These controller design approaches are sensitive to unknown exogenous disturbances, unknown model uncertainties, and plant parameter variations that may develop instability in the closed-loop system. Assimilation of erroneous control efforts fundamentally induces instability, producing divergence in the systems' state variables. Termination of diverging synchronization error signals requires high energy control efforts.

Objective 1: To construct a feedback control algorithm that synthesizes a control input $\mathbf{u}(t) \in R^{3\times 1}$, which establishes faster and smooth synchronization error vector (10) convergence to zero with lesser fluctuations in the error and feedback control signals.

This work proposes a novel robust adaptive controller design methodology that does not eliminate the closed-loop's nonlinear terms, making it independent of chaotic RCLSJJ system parameters. The proposed strategy synthesizes less active control signals. It enforces the synchronization error vector (10) to zero smoothly. This controller uses real-time estimates of unknown model uncertainties and bounds to compensate for unknown exogenous disturbances.

The following section discusses the structure of the proposed controller to address the problems elaborated in the above critique; it develops a design procedure based on the Lyapunov stability analysis theory.

V. A SOLUTION TO THE PROBLEM

A. CONTROLLER DESIGN AND PARAMETERS UPDATE LAWS

Theorem: The feedback control input $\mathbf{u}(t) \in R^{3\times 1}$ computed using control law (14) realizes global asymptotic synchronization between master and slave chaotic RCLSJJ systems given in (5-6).

$$
\mathbf{u}(t) = -\mathbf{A}\mathbf{e}(t) - (\mathbf{B}(t) + \widehat{\boldsymbol{\Psi}}(t))\,\mathrm{sign}(\mathbf{e}(t)), \qquad (14)
$$

where $\hat{\boldsymbol{\Psi}}(t)$ is an unknown controller parameter and, $\hat{\boldsymbol{\Psi}}(t) = \hat{\boldsymbol{\Phi}}(t) + \hat{\boldsymbol{\Gamma}}(t)$.

Remark 2: The control input (14) has three distinct components, each of which plays a specific role, summarized as follows.

(i) The suitable selection of the matrix $\mathbf{A}$ diagonal assures the closed-loop (10) linear part stability.

(ii) Mathematical analysis shows that $\mathbf{B}(t)\,\mathrm{sign}(\mathbf{e}(t))$ takes care of reducing the nonlinearity effects. The parameter $\mathbf{B}(t)$ makes the controller heuristic because $\lim_{\mathbf{e}(t)\to 0} \mathbf{B}(t) = 0$. Hence, in the vicinity of zero, $\mathbf{B}(t)$ exerts a negligible influence on the control effort, whereas $\mathbf{B}(t)$ plays a pivotal role in substantial deviations. Consequently, $\mathbf{B}(t)$ strongly penalizes significant deviations while exhibiting a more subdued response to minor deviations, thereby yielding a seamless synthesis of control signals in the proximity of zero and a more pronounced one elsewhere.

(iii) The term $\hat{\boldsymbol{\Psi}}(t)\,\mathrm{sign}(\mathbf{e}(t))$ compensates time-varying exogenous disturbances and model uncertainties.

(iv) Analysis of the computer simulation results shows that $\left(\mathbf{B}(t) + \hat{\boldsymbol{\Psi}}(t)\right)\mathrm{sign}(\mathbf{e}(t))$ achieves smooth, fast state error trajectories convergence to zero, and the error signals are less oscillatory.

B. CLOSED-LOOP ANALYSIS

Proof: Consider

$$
V(\mathbf{e}(t)) = \frac{1}{2}\mathbf{e}^T(t)\mathbf{e}(t) + \frac{\sigma}{2}\tilde{\boldsymbol{\Psi}}_D^T(t)\tilde{\boldsymbol{\Psi}}_D(t) \geq 0, \qquad (15)
$$

where $\tilde{\boldsymbol{\Psi}}_D(t) = \boldsymbol{\Psi}_D - \hat{\boldsymbol{\Psi}}_D(t)$, and $\hat{\boldsymbol{\Psi}}_D(t)$ and $\tilde{\boldsymbol{\Psi}}_D(t)$ are vectors representing diagonals of $\hat{\boldsymbol{\Psi}}(t)$ and $\tilde{\boldsymbol{\Psi}}(t)$, respectively. Now,

$$
\dot{V}(\mathbf{e}(t)) = \mathbf{e}^T(t)\,\dot{e}(t) - \sigma\tilde{\boldsymbol{\Psi}}_D^T(t)\,\dot{\hat{\boldsymbol{\Psi}}}_D(t). \qquad (16)
$$

Using (10) and (14) into (16) yields:

$$
\begin{aligned}
\dot{V}(\mathbf{e}(t)) = {} & \mathbf{e}^T(t)\left(\begin{bmatrix} 0 & 1 & 0 \\ 0 & -a_1a_3 & -a_1 \\ 0 & a_2 & -a_2 \end{bmatrix}\right)\mathbf{e}(t) \\
& + \mathbf{e}^T(t)\begin{bmatrix} 0 \\ e_1(t)\cos\theta(t) \\ 0 \end{bmatrix} - \mathbf{e}^T(t)\mathbf{A}\mathbf{e}(t) \\
& - \mathbf{e}^T(t)\mathbf{B}(t)\,\mathrm{sign}(\mathbf{e}(t)) - \sigma\tilde{\boldsymbol{\Psi}}_D^T(t)\hat{\boldsymbol{\Psi}}_D(t) \\
& + \mathbf{e}^T(t)\left(\boldsymbol{\Psi}_D^{ms}\left(\boldsymbol{\Phi}_D^{ms}\left(\mathbf{x}^{ms}(t)\right), \boldsymbol{\Gamma}_D^{ms}(t)\right)\right) \\
& - \mathbf{e}^T(t)\widehat{\boldsymbol{\Psi}}^{ms}(t)\,\mathrm{sign}(\mathbf{e}(t)) \\
= {} & -a_1a_3e_2^2(t) - a_2e_3^2(t) - a_1e_1(t)e_2(t)\cos\theta(t) \\
& + e_1(t)e_2(t) + (a_2 - a_1)\,e_2(t)e_3(t) \\
& - \mathbf{e}^T(t)\mathbf{A}\mathbf{e}(t) - \mathbf{e}^T(t)\mathbf{B}(t)\,\mathrm{sign}(\mathbf{e}(t)) \\
& + \mathbf{e}^T(t)\left(\boldsymbol{\Psi}_D^{ms}\left(\boldsymbol{\Phi}_D^{ms}\left(\mathbf{x}^{ms}(t)\right), \boldsymbol{\Gamma}_D^{ms}(t)\right)\right) \\
& - \mathbf{e}^T(t)\widehat{\boldsymbol{\Psi}}^{ms}(t)\,\mathrm{sign}(\mathbf{e}(t)) - \sigma\tilde{\boldsymbol{\Psi}}_D^T(t)\hat{\boldsymbol{\Psi}}_D(t) \\
= {} & -\mathbf{e}^T(t)\mathbf{P}\mathbf{e}(t) + \mathbf{e}^T(t)\mathbf{M}(t)\mathbf{e}(t) \\
& - \mathbf{e}^T(t)\mathbf{A}\mathbf{e}(t) - \mathbf{e}^T(t)\mathbf{B}(t)\,\mathrm{sign}(\mathbf{e}(t)) \\
& + \mathbf{e}^T(t)\left(\boldsymbol{\Psi}_D^{ms}\left(\boldsymbol{\Phi}_D^{ms}\left(\mathbf{x}^{ms}(t)\right), \boldsymbol{\Gamma}_D^{ms}(t)\right)\right)
\end{aligned}
$$

$$
\begin{aligned}
&- \mathbf{e}^T(t)\widehat{\boldsymbol{\Psi}}^{ms}(t)\,\mathrm{sign}(\mathbf{e}(t)) - \sigma\widetilde{\boldsymbol{\Psi}}_D^T(t)\hat{\boldsymbol{\Psi}}_D(t)\\
&= -\mathbf{e}^T(t)\mathbf{P}\mathbf{e}(t) + \mathbf{e}^T(t)\mathbf{M}(t)\mathbf{e}(t)\\
&\quad - \mathbf{e}^T(t)\mathbf{A}\mathbf{e}(t) - \mathbf{e}^T(t)\mathbf{B}(t)\,\mathrm{sign}(\mathbf{e}(t))\\
&\quad + \mathbf{e}^T(t)\left(\boldsymbol{\Psi}_D^{ms}\left(\boldsymbol{\phi}_D^{ms}\left(\mathbf{x}^{ms}(t)\right),\boldsymbol{\Gamma}_D^{ms}(t)\right)\right)\\
&\quad - \mathbf{e}^T(t)\widehat{\boldsymbol{\Psi}}^{ms}(t)\,\mathrm{sign}(\mathbf{e}(t)) - \sigma\widetilde{\boldsymbol{\Psi}}_D^T(t)\hat{\boldsymbol{\Psi}}_D(t)\\
&= -\mathbf{e}^T(t)\mathbf{Q}(t)\mathbf{e}(t) - \mathbf{e}^T(t)\mathbf{B}(t)\,\mathrm{sign}(\mathbf{e}(t))\\
&\quad + \mathbf{e}^T(t)\left(\boldsymbol{\Psi}_D^{ms}\left(\boldsymbol{\phi}_D^{ms}\left(\mathbf{x}^{ms}(t)\right),\boldsymbol{\Gamma}_D^{ms}(t)\right)\right)\\
&\quad - \mathbf{e}^T(t)\widehat{\boldsymbol{\Psi}}^{ms}(t)\,\mathrm{sign}(\mathbf{e}(t)) - \sigma\widetilde{\boldsymbol{\Psi}}_D^T(t)\hat{\boldsymbol{\Psi}}_D(t)\\
&\le -\mathbf{e}^T(t)\mathbf{Q}(t)\mathbf{e}(t) - \mathbf{e}^T(t)\mathbf{B}(t)\,\mathrm{sign}(\mathbf{e}(t))\\
&\quad + \left|\mathbf{e}^T(t)\left(\boldsymbol{\Psi}_D^{ms}\left(\boldsymbol{\phi}_D^{ms}\left(\mathbf{x}^{ms}(t)\right),\boldsymbol{\Gamma}_D^{ms}(t)\right)\right)\right|\\
&\quad - \left|\mathbf{e}^T(t)\right|\widehat{\boldsymbol{\Psi}}_D^{ms}(t) - \sigma\widetilde{\boldsymbol{\Psi}}_D^T(t)\hat{\boldsymbol{\Psi}}_D(t)\\
&\le -\mathbf{e}^T(t)\mathbf{Q}\mathbf{e}(t) - \mathbf{e}^T(t)\mathbf{B}(t)\,\mathrm{sign}(\mathbf{e}(t))\\
&\quad + \left|\mathbf{e}^T(t)\right|\left|\boldsymbol{\Psi}_D^{ms}\left(\boldsymbol{\Phi}_D^{ms}\left(\mathbf{x}^{ms}(t)\right),\boldsymbol{\Gamma}_D^{ms}(t)\right)\right|\\
&\quad - \left|\mathbf{e}^T(t)\right|\widehat{\Psi}_D^{ms}(t) - \sigma\widetilde{\boldsymbol{\Psi}}_D^T(t)\hat{\boldsymbol{\Psi}}_D(t), \qquad (17)
\end{aligned}
$$

where $\mathbf{e}^T(t)\,\mathrm{sign}(\mathbf{e}(t)) = |\mathbf{e}(t)|$. Using Assumption 1 in (17) yields:

$$
\begin{aligned}
\dot{V}(\mathbf{e}(t)) &\le -\mathbf{e}^T(t)\mathbf{Q}\mathbf{e}(t) - \mathbf{e}^T(t)\mathbf{B}(t)\,\mathrm{sign}(\mathbf{e}(t))\\
&\quad + \left|\mathbf{e}^T(t)\right|\boldsymbol{\Psi}_D - \left|\mathbf{e}^T(t)\right|\widehat{\boldsymbol{\Psi}}_D^{ms}(t) - \sigma\widetilde{\boldsymbol{\Psi}}_D^T(t)\hat{\boldsymbol{\Psi}}_D(t)\\
&\le -\mathbf{e}^T(t)\mathbf{Q}\mathbf{e}(t) - \mathbf{e}^T(t)\mathbf{B}(t)\,\mathrm{sign}(\mathbf{e}(t))\\
&\quad + \left|\mathbf{e}^T(t)\right|\left(\boldsymbol{\Psi}_D - \widehat{\boldsymbol{\Psi}}_D^{ms}(t)\right) - \sigma\widetilde{\boldsymbol{\Psi}}_D^T(t)\hat{\boldsymbol{\Psi}}_D(t)\\
&\le -\mathbf{e}^T(t)\mathbf{Q}\mathbf{e}(t) - \mathbf{e}^T(t)\mathbf{B}(t)\,\mathrm{sign}(\mathbf{e}(t))\\
&\quad + \left|\mathbf{e}^T(t)\right|\widetilde{\boldsymbol{\Psi}}_D(t) - \sigma\widetilde{\boldsymbol{\Psi}}_D^T(t)\hat{\boldsymbol{\Psi}}_D(t)\\
&\le -\mathbf{e}^T(t)\mathbf{Q}(t) - \mathbf{e}^T(t)\mathbf{B}(t)\,\mathrm{sign}(\mathbf{e}(t))\\
&\quad + \widetilde{\boldsymbol{\Psi}}_D^T(t)\left(|\mathbf{e}(t)| - \sigma\hat{\boldsymbol{\Psi}}_D(t)\right), \qquad (18)
\end{aligned}
$$

where

$$
\mathbf{Q}(t) = \mathbf{A} + \mathbf{P} - \mathbf{M}(t),
$$

$$
\mathbf{A} = \begin{bmatrix} \alpha_{11} & 0 & 0\\ 0 & \alpha_{22} & 0\\ 0 & 0 & \alpha_{33}\end{bmatrix},
$$

$$
\mathbf{P} = \begin{bmatrix} 0 & 0 & 0\\ 0 & a_1a_3 & 0\\ 0 & 0 & a_2\end{bmatrix},
$$

$$
\mathbf{M}(t) = \begin{bmatrix} 0 & 1-a_1\cos\theta(t) & 0\\ 0 & 0 & a_2-a_1\\ 0 & 0 & 0\end{bmatrix},
$$

and

$$
(1-a_1\cos\theta(t))e_1(t)e_2(t) + (a_2-a_2)e_2(t)e_3(t) = \mathbf{e}^T(t)\mathbf{M}(t)\mathbf{e}(t).
$$

To assure $\dot{V}(\mathbf{e}(t))$ remains negative in Eq. (18), consider $|\mathbf{e}(t)| - \sigma\dot{\hat{\boldsymbol{\Psi}}}_D(t) = 0$; therefore, we may write,

$$
\dot{\hat{\boldsymbol{\Psi}}}_D(t) = \frac{1}{\sigma}|\mathbf{e}(t)|, \quad \hat{\boldsymbol{\Psi}}_D(0) = \hat{\boldsymbol{\Psi}}_{D0}. \qquad (19)
$$

TABLE 2. Initial conditions, RCLSJJ chaotic system parameters, controller parameters, and model uncertainties.

Initial conditions[1]	Parameters of the RCLSJJ system [15]	Parameters of the controller (14)	Model uncertainties[2]
$x_1^m(0) = -0.5$, $x_2^m(0) = 1$, $x_3^m(0) = 1$, $x_1^s(0) = -1$, $x_2^s(0) = 2.5$, $x_3^s(0) = 1.7$, $\hat{\psi}_{110} = 0.2$, $\hat{\psi}_{220} = 0.4$, $\hat{\psi}_{330} = 0.6$	$a_1 = 1.4144$, $a_2 = 0.3731$, $a_3 = 0.0478$, $a_4 = 1.2$	$\alpha_{ii} = 1$, $\eta_{ii} = 1$, $\sigma = 0.55$, $\rho = 0.01$, $\varrho = 0.01$,	$\phi_{11}^m(x_1^m(t)) = 0.3\sin 4x_1^m(t)$, $\phi_{22}^m(x_2^m(t)) = -0.2\cos 2x_2^m(t)$, $\phi_{33}^m(x_3^m(t)) = 0.1\sin 4x_3^m(t)$, $\phi_{11}^s(x_4^s(t)) = 0.15\sin 4x_1^s(t)$, $\phi_{22}^s(x_2^s(t)) = 0.1\sin 2x_2^s(t)$, $\phi_{33}^s(x_3^s(t)) = 0.15\cos x_3^s(t)$

1. A set of initial conditions developed chaos in the RCLSJJ system.
2. Sinusoidal functions are simple periodic functions that provide a good estimation of many real-world physical disturbances and model uncertainties associated with dynamical systems. These functions are suitable for modelling oscillations or variations in RCLSJJ systems due to internal and/or external factors.

Equation (19) is an adaptive law that estimates controller parameters for the compensation of unknown uncertainties and exogenous disturbances $\hat{\boldsymbol{\Psi}}(t) = \hat{\boldsymbol{\phi}}(t) + \hat{\boldsymbol{\Gamma}}(t)$, where $\hat{\boldsymbol{\Psi}}_{D0}$ is the initial value of $\hat{\boldsymbol{\Psi}}_D(t)$.

Using the controller parameters estimate laws (19) into (18) implies:

$$
\dot{V}(\mathbf{e}(t)) \le -\mathbf{e}^T(t)\mathbf{Q}\mathbf{e}(t) - \mathbf{e}^T(t)\mathbf{B}(t)\,\mathrm{sign}(\mathbf{e}(t)) \qquad (20)
$$

Let us choose $\alpha_{ii} > 0$, $\eta_{ii}>0$, and $0 < \rho \le 1$, which assures that $\mathbf{e}^T(t)\mathbf{B}(t)\,\mathrm{sign}(\mathbf{e}(t)) \ge 0$ and $\mathbf{Q}(t) > 0$; consequently $\dot{V}(\mathbf{e}(t)) \le 0$.

Remark 3: The inequality (20) determines that the error vector trajectories (10) converge to the origin. The unknown controller parameter estimations are associated with the exogenous disturbances and uncertainties and approach some constant values. Hence, the closed-loop (10) global asymptotic stability is proved [34]; it establishes that $\lim_{t\to\infty}\|\mathbf{e}(t)\| = 0$. □

Remark 4: The feedback controller gains are computed as $\alpha_{11} > 0$, $\alpha_{22} > 0$, and $\alpha_{33} > 0$, where the constants are chosen as $\eta_{ii} > 0$, $\varrho \ge 0$, and $0 < \rho \le 1$ that assures $\eta_{ii}\left(1 - \rho e^{-\varrho|e_i(t)|}\right) \ge 0$.

Remark 5: The controller parameters $\alpha_{ii}\eta_{ii}$, and ϱ regulate the error decay rate. Figures 8(a-d) depict that the synchronization speed increases for large values of α_{ii} and η_{ii}, and small values of ϱ.

VI. NUMERICAL SIMULATIONS AND COMPARATIVE STUDY

Table 2 gives information about the initial conditions, RCLSJJ chaotic system parameters, controller parameters, and model uncertainties in numerical simulations. All differ-

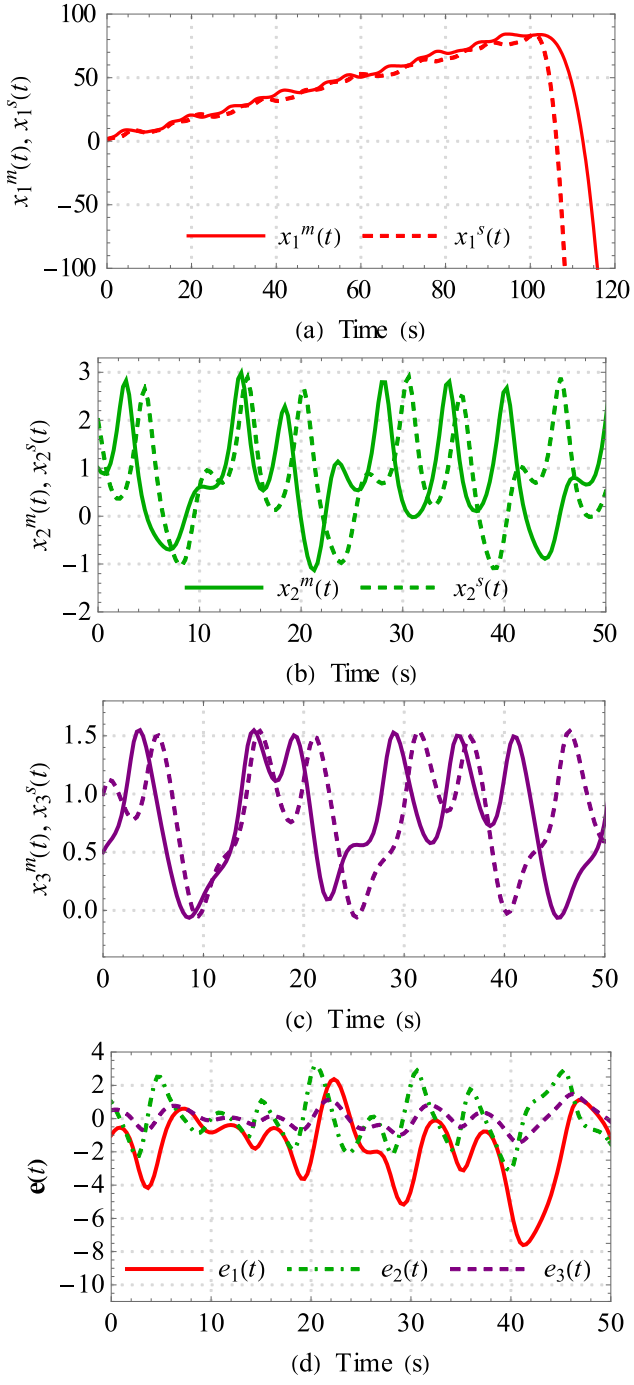

FIGURE 5. State variable trajectories behaviour, (a) $x_1^m(t)$ and $x_1^s(t)$, (b) $x_2^m(t)$ and $x_2^s(t)$, and (c) $x_3^m(t)$ and $x_3^s(t)$, and (d) error vector behaviour.

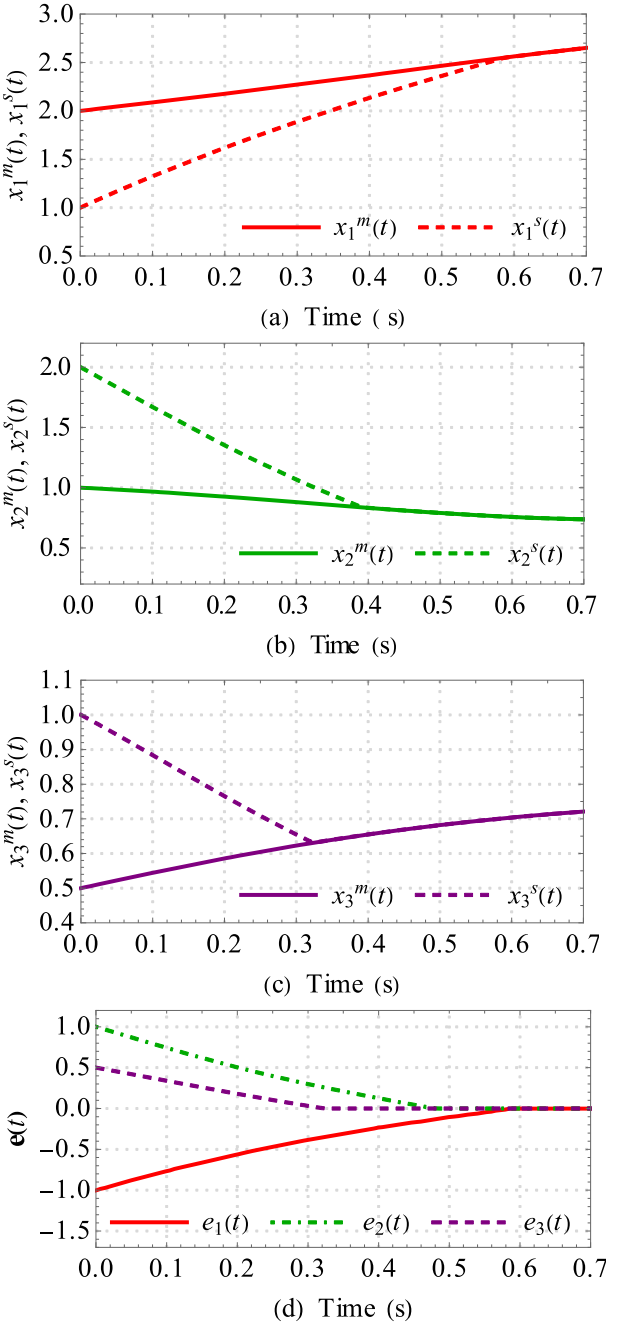

FIGURE 6. Using the control effort (14), State variable trajectories behaviour, (a) $x_1^m(t)$ and $x_1^s(t)$, (b) $x_2^m(t)$ and $x_2^s(t)$, and (c) $x_3^m(t)$ and $x_3^s(t)$, and (d) error vector behaviour.

ential equations are simulated using the Explicit Runge-Kutta method [42] in *Mathematica* 12.0 v.

The state-variable trajectories $x_i(t)$, $i = 1, 2, 3$ in Figures 5(a-c) and error vector trajectories in Figure 5(d) demonstrate that the MSS arrangement (5-6) does not synchronize without any control effort.

Example 1: The simulation results in Figures 6(a-d) and 7 are performed using the proposed RDASCS (14). Figures 6(a-c) demonstrate that the corresponding state variables $x_i^m(t)$ and $x_i^s(t)$ $(i = 1, 2, 3)$ trajectories of the MSS (5-6) show similar behaviour after a short transient time. The error trajectories converge to the origin smoothly, as shown in Figure 6(d). Figure 7 depicts the estimated parameter $\hat{\dot{\Psi}}(t)$ convergence using the parameter update laws (19).

Example 2: This example studies the controller parameters α_{ii}, η_{ii}, and σ effects on the convergence time.

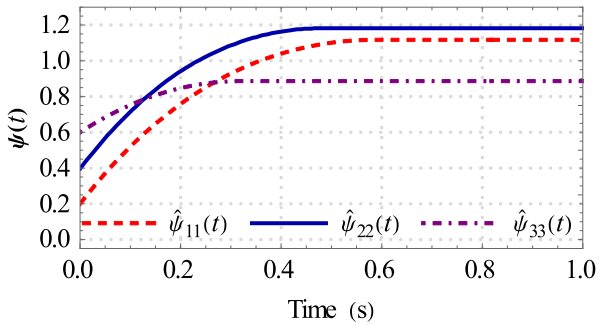

FIGURE 7. Convergence of the estimated parameter, $\dot{\hat{\Psi}}(t) = \dot{\hat{\Phi}}(t) + \dot{\hat{\Gamma}}(t)$.

The convergence behaviour of the error vector for different controller parameters α_{ii}, η_{ii}, and σ are shown in Figures 8(a-d). These figures demonstrate an increasing trend in the error's speed convergence for large values of α_{ii} & η_{ii} and small values of σ.

A. COMPARATIVE ANALYSIS

This subsection compares the performance of the proposed method for analyzing the efficiency of RDASCS (14) with state-of-the-art control techniques [32], [35].

The state-feedback control input vector $\mathbf{u}(t) \in R^{3\times 1}$ synthesized by the benchmark methodologies, namely adaptive control technique (ACT) [32] and sliding mode control (SMC) strategy [35], as given in (21) and (23), respectively. Further, all simulations considered the same initial conditions and preliminary controller parameters presented in Table 2.

i) Adaptive control technique [32]:

$$\mathbf{u}(t) = -\left(\mathbf{A} + \begin{bmatrix} 0 & 1 & 0 \\ 0 & \hat{a}_1(t)\hat{a}_3(t) & \hat{a}_1(t) \\ 0 & -\hat{a}_2(t) & \hat{a}_2(t) \end{bmatrix}\right)\begin{bmatrix} e_1(t) \\ e_2(t) \\ e_3(t) \end{bmatrix} + \begin{bmatrix} 0 \\ a_1\left(\sin x_1^s(t) - \sin x_1^m(t)\right) \\ 0 \end{bmatrix} - \mathbf{K}(t)\begin{bmatrix} e_1(t) \\ e_2(t) \\ e_3(t) \end{bmatrix} \tag{21}$$

where $\mathbf{K} = \text{diag}\left[d_{ij}(t), i \neq j \Rightarrow d_{ij}(t) = 0, i, j = 1, 2, 3\right]_{3\times 3}$ and $d_{11}(t) = \frac{k_1}{l\left(|e_1(t)| + k_2 e^{-k_3 t}\right)}$, $d_{22}(t) = \frac{k_1}{l\left(|e_2(t)| + k_2 e^{-k_3 t}\right)}$, and $d_{33}(t) = \frac{k_1}{l\left(|e_2(t)| + k_2 e^{-k_3 t}\right)}$, $\mathbf{A} = \left\{\alpha_{ij}, i \neq j \Rightarrow \alpha_{ij} = 0\right\} \in R^{3\times 3} (i, j = 1, 2, 3)$ is the feedback controller gains matrix, and l are positive real constants. $\hat{a}_i(t)\,(i = 1, 2, 3)$ are the parameters updated according to the following adaptation laws [32].

$$\begin{cases} \dot{\hat{a}}_1(t) = -k_4\left(k_5 |e_1(t)|\right)\hat{a}_1(t) + k_1 e_2(t) e_2(t) \\ \dot{\hat{a}}_2(t) = -k_4\left(k_5 |e_2(t)|\right)\hat{a}_2(t) - k_2 e_2^2(t) - k_3 e_3^2(t) \\ \dot{\hat{a}}_3(t) = -k_4\left(k_5 |e_3(t)|\right)\hat{a}_3(t) \end{cases} \tag{22}$$

ii) Sliding mode control strategy [35]:

$$\mathbf{u}(t) = \left(\mathbf{A} + \begin{bmatrix} 0 & 1 & 0 \\ 0 & -a_1 a_3 & -a_1 \\ 0 & a_2 & -a_2 \end{bmatrix}\right)\begin{bmatrix} e_1(t) \\ e_2(t) \\ e_3(t) \end{bmatrix}$$

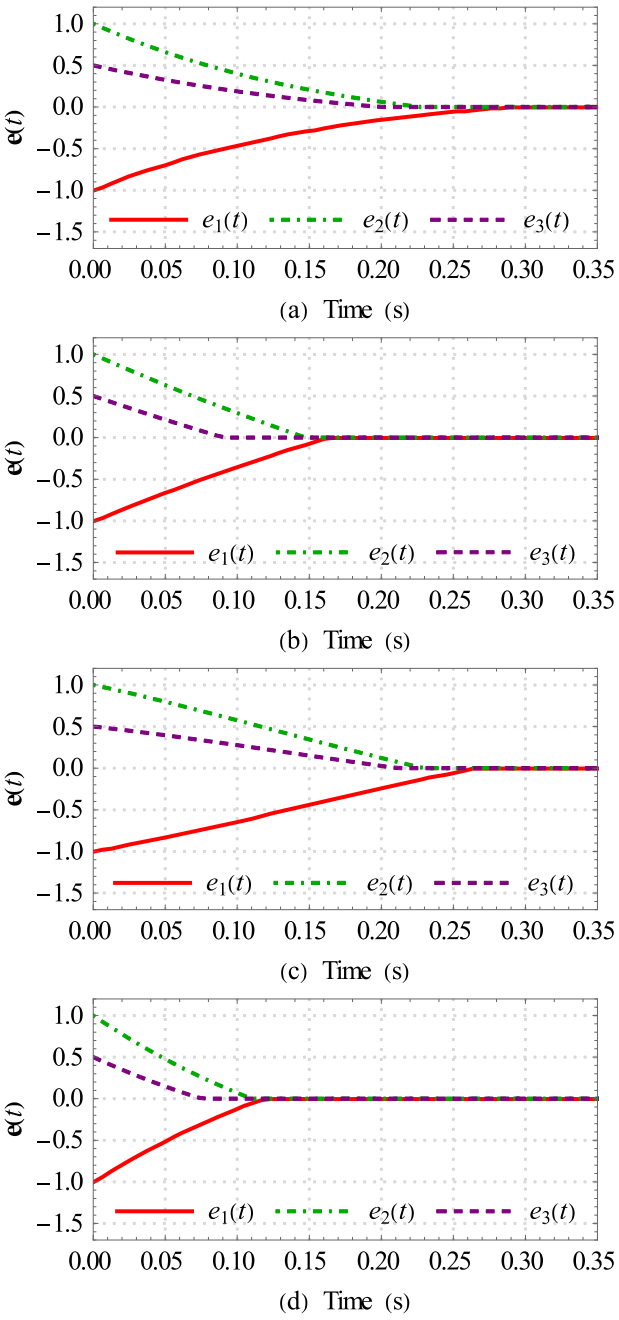

FIGURE 8. Errors vector behaviour with a control effort (14) when (a) $\alpha_{ii} = 5$, $\eta_{ii} = 1$, $\sigma = 0.55$ (b) $\alpha_{ii} = 1$, $\eta_{ii} = 5$, $\sigma = 0.55$, (c) $\alpha_{ii} = 1$, $\eta_{ii} = 1$, $\sigma = 0.1$, and (d) $\alpha_{ii} = 5$, $\eta_{ii} = 5$, $\sigma = 0.1$.

$$+ \begin{bmatrix} 0 \\ -x_3^m(t)e_1(t) - x_3^s(t)e_3(t) \\ \left(x_1^m(t) + x_1^s(t)\right)e_1(t) \end{bmatrix} - \eta\begin{bmatrix} \text{sgn}\left(c_1 e_1(t)\right) \\ \text{sgn}\left(c_2 e_2(t)\right) \\ \text{sgn}\left(c_3 e_3(t)\right) \end{bmatrix} \tag{23}$$

where $\eta = \text{diag}\left[\eta_{ij}, i \neq j \Rightarrow \eta_{ij} = 0\right] \in R^{3\times 3}$, and $\mathbf{A} = \left\{\alpha_{ij}, i \neq j \Rightarrow \alpha_{ij} = 0\right\} \in R^{3\times 3} (i, j = 1, 2, 3)$ are the feedback controller gains matrices, and $c > 0$ is any real constant [35].

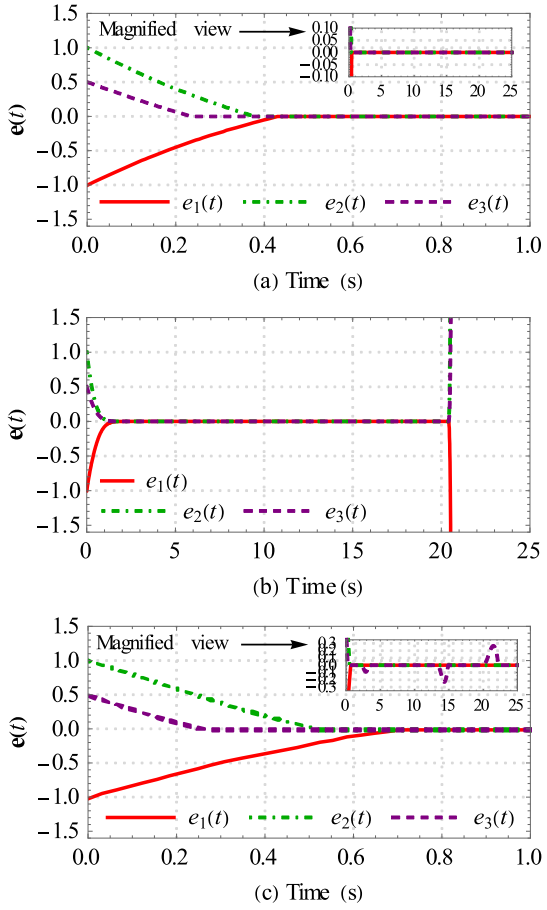

FIGURE 9. Error vector behaviour by the (a) proposed controller (14), (b) adaptive controller (21), and (c) SMC strategy (23).

TABLE 3. Comparison of computer simulation results.

Control input/Feed back gains	Figure No/ Error convergence time	Range of the error oscillations in the steady-state	Figure No/ Range of the control signals fluctuations in the steady-state
RDASCS (14)	Figure 9(a)/0.41s	Less active oscillations	Figure 10(a)/ Reduced oscillations
ACT (21) $\alpha_{ii}=1$, $i=1,2,3$, $l=1$, $k_1=1$, $k_j=0.4$, $j=2,3,4$	Figure 9(b)/ does not establish synchronization	It does not establish synchronization	Figure 10(b)/ Diverges
SMC strategy (23) $\alpha_{ii}=1$, $\eta_{ii}=1$, $\gamma_{ii}=1$, $c_i=1$, for $i=1,2,3$	Figure 9(c)/0.7s	Steady-state oscillations in the range $[-0.15, 0.15]$	Figure 10(c)/ Oscillate in the range $[-0.4, 0.9]$

Example 3: Assume no exogenous disturbances and model uncertainties act on the MSS (5-6). Figures 9(a-c)

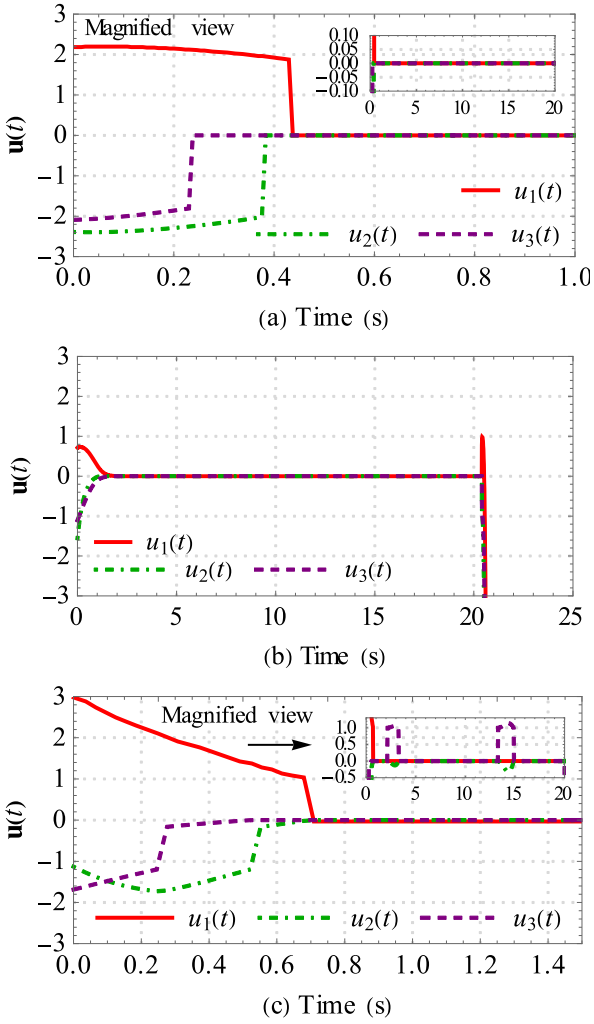

FIGURE 10. The transient behaviour of the (a) proposed control signals (14), (b) adaptive control signals (21), and (c) SMC signals (23).

depict the error vector convergence behaviour accomplished by the proposed RDASCS (14), ACT (21) and SMC strategy (23), alternatively. These figures demonstrate that the proposed RDASCS (14) establishes the synchronization in less than 0.42 seconds with reduced oscillations. Figure 9(b) shows that the controllers in (21) achieve the synchronization behaviour in 1.6 seconds, while SMC strategy (23) realizes the synchronization behaviour in 0.7 seconds with some irregular jumps in the steady state, as shown in Figure 9 (c).

The proposed controller (14) synthesizes a smooth control effort, as shown in Figure 10(a); it takes appropriate action to compel the state error vector to the origin. The control signals of the ACT (21) are smooth but have a longer convergence time due to the small initial amplitude of the control effort, as illustrated in Figure 10(b). The SMC signals (23) exhibit fluctuating behaviour in the range $[-0.4, 1.2]$, as shown in Figure 10(c).

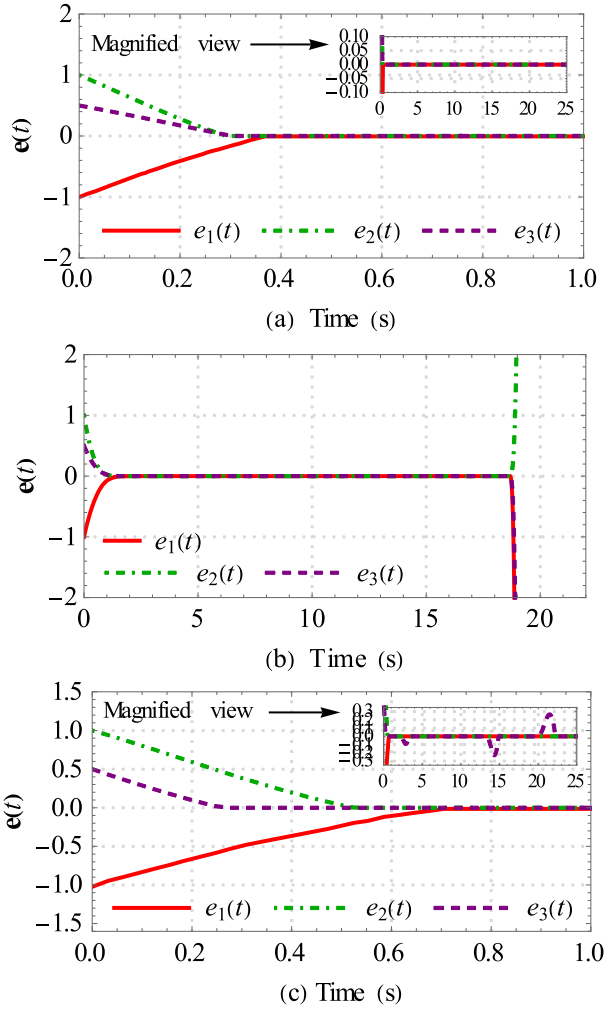

FIGURE 11. Scenario 1: Error vector behaviour by the (a) RDASCS (14), (b) adaptive controller (21), and (c) SMC strategy (23).

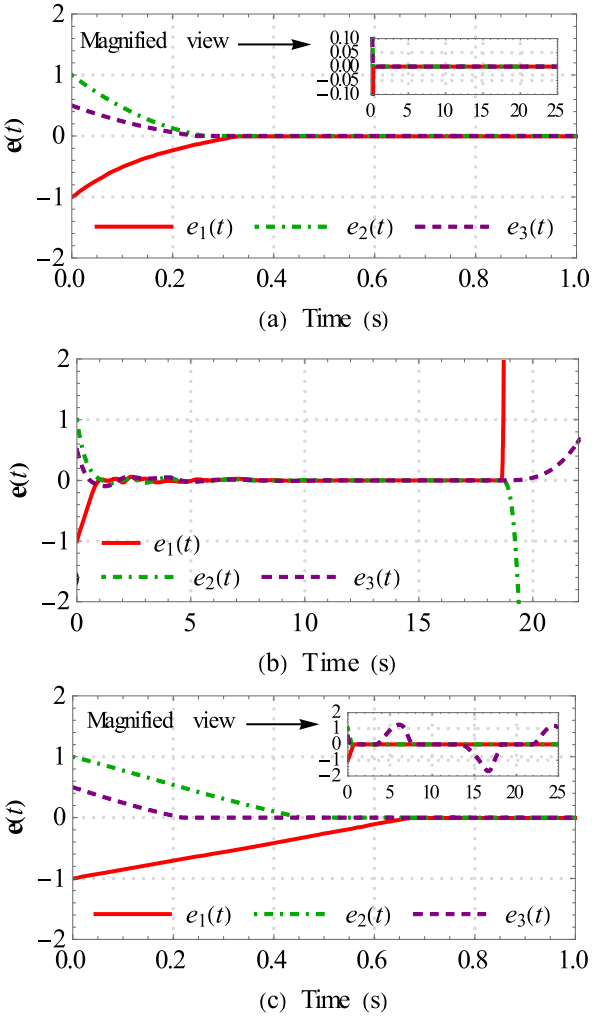

FIGURE 12. Scenario 2: Error vector behaviour by the (a) RDASCS (14), (b) adaptive controller (21), and (c) SMC strategy (23).

The closed-loop (10) key performance indicators are summarized in Table 3 for comparative analysis, shown in Figures 9(a-c)-10(a-c).

B. CLOSED-LOOP ROBUSTNESS ANALYSIS COMPARISON

Example 4: This example studies and compares the effects of 10% smooth system parameters variations, exogenous disturbances and model uncertainties and their combined effect on the closed-loop performance of the proposed RDASCS (14) and controllers (21, 23).

Scenario 1: Effects of 10% smooth system parameters variations

$$a_1 = 1.4144 + 0.141\, e^{-0.01\,t}, \quad a_2 = 0.3731 + 0.037\, e^{-0.01\,t}$$
$$a_3 = 0.0478 + 0.0048\, e^{-0.01\,t}, \quad a_4 = 1.2 + 0.12\, e^{-0.01\,t} \tag{24}$$

Scenario 2: Effects of model uncertainties and exogenous disturbances

i). Model uncertainties

$$\begin{aligned} \phi_{11}^m\left(x_1^m(t)\right) &= 0.3\sin 4\, x_1^m(t), \\ \phi_{22}^m\left(x_2^m(t)\right) &= -0.4\cos 2\, x_2^m(t) \\ \phi_{33}^m\left(x_3^m(t)\right) &= 0.2\sin 2\, x_3^m(t), \quad \phi_{11}^s\left(x_1^s(t)\right) = 0.2\cos 4\, x_1^s(t), \\ \phi_{22}^s\left(x_2^s(t)\right) &= -0.1\sin 4\, x_2^s(t), \quad \phi_{33}^s\left(x_3^s(t)\right) = 0.3\sin 5\, x_3^s(t) \end{aligned} \tag{25}$$

ii). Exogenous disturbances

$$\begin{aligned} \delta_{ii}^m(t) &= 0.2\sin\left(0.1\pi t + \frac{\pi}{3}\right), \\ \delta_{ii}^s(t) &= 0.3\sin\left(0.1\pi t + \frac{\pi}{5}\right), \quad i = 1, 2, 3 \end{aligned} \tag{26}$$

Scenario 3: Combined effects of 10% smooth parameter variations (24), model uncertainties (25), and exogenous disturbances (26).

Figures 11(a-c), 12(a-c), and 13(a-c) illustrate the error trajectories' convergence behaviours and the control signal

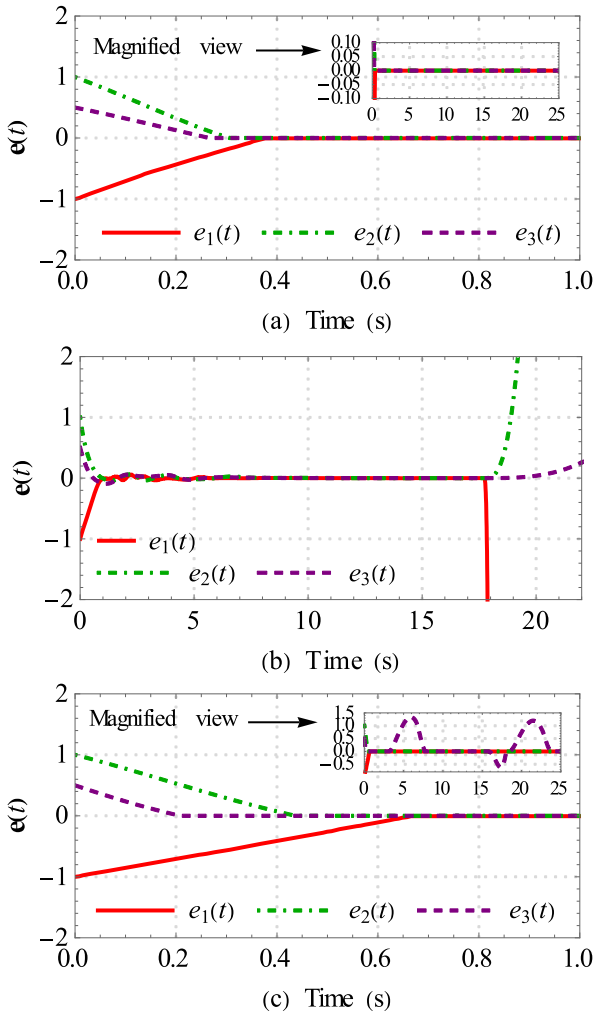

FIGURE 13. Scenario 3: Error vector behaviour by the (a) RDASCS (14), (b) adaptive controller (21), and (c) SMC strategy (23).

behaviours to zero are shown in Figures 14(a-c), 15(a-c), and 16(a-c) established by the proposed RDASCS (14), ACT (21), and SMC strategy (23) for Scenarios 1 to 3, alternatively. Table 4 summarizes the error and control signals attitudes appearing in simulation results (Figures 11(a-c) to 16(a-c)) for performance analysis. Data in this table concludes that the proposed controller performs better in the error convergence and synthesis of the control signals among the selected benchmark methodologies.

The following figures show the comparative simulation results of the error trajectories behaviour by the controllers (14), (21), and (23) for Scenarios 1-3.

The following figures show the comparative simulation results of the control efforts by the controllers (14), (21), and (23) for Scenarios 1-3.

Data in Table 5 verify that the proposed method achieves a better error convergence attitude according to the standard error convergence performance indices. It shows that compared to the proposed RDASCS (14), the values of *IAE, ITAE, ISE*, and *ITSE* [43] are higher for the controllers (21, 23). The simulation duration is $T_s = 20$ seconds.

Figures 17(a-b) represent the behaviour of $\mathbf{E}(t) = \mathbf{E}_1(t) = \mathbf{E}_2(t) = \mathbf{e}^T(t)\,\mathbf{e}(t)$ by the proposed method (14),

TABLE 4. Comparison of computer simulation results.

Feedback controller	Scenario	Figure No/ Error convergence time	Range of the error oscillations in the steady-state	Figure No/ Range of the control signals oscillations
RDASCS (14)	Scenario 1	Figure 11(a)/0.4s	Less active oscillations	Figure 14(a)/ Reduced oscillations
	Scenario 2	Figure 12(a)/0.38s	Less active oscillations	Figure 15(a)/ Reduced oscillations
	Scenario 3	Figure 13(a)/0.38s	Less active oscillations	Figure 16(a)/ Reduced oscillations
ACT (21)	Scenario 1	Figure 11(b)/ does not establish synchronization	Diverges	Figure 14(b)/ Diverges
	Scenario 2	Figure 12(b)/ does not establish synchronization	Diverges	Figure 15(b)/ Diverges
	Scenario 3	Figure 13(b)/ does not establish synchronization	Diverges	Figure 16(b)/ Diverges
SMC strategy (23)	Scenario 1	Figure 11(c)/0.7s	Fluctuations in the steady state in the range of $[-0.4, 0.4]$	Figure 14(c)/ Oscillate in the range of $[-1.6, 1.5]$
	Scenario 2	Figure 12(c)/0.7s	Fluctuations in the steady state in the range of $[-1.5, 1.2]$	Figure 15(c)/ Oscillate in the range of $[-2.5, 2.2]$
	Scenario 3	Figure 13(c)/0.7s	Fluctuations in the steady state in the range of $[-0.5, 1.5]$	Figure 16 (c)/ Oscillate in the range of $[-2, 2]$

TABLE 5. Comparison of *IAE, ITAE, ISE*, and *ITSE*.

Index	Error	RDASCS (14)	ACT (21)	SMC (23)
$IAE = \int_0^{Ts} \lvert\mathbf{e}(t)\rvert dt$	$e_1(t)$	0.1939	0.4371	0.3194
	$e_2(t)$	0.1484	0.3652	0.2121
	$e_3(t)$	0.0625	0.1935	5.9088
$ITAE = \int_0^{Ts} \lvert\mathbf{e}(t)\rvert t\, dt$	$e_1(t)$	0.0263	0.1546	0.0682
	$e_2(t)$	0.0152	0.1131	0.0301
	$e_3(t)$	0.0052	0.0612	66.739
$ISE = \int_0^{Ts} \mathbf{e}^T(t)\mathbf{e}(t)dt$	$e_1(t)$	0.1234	0.2489	0.2124
	$e_2(t)$	0.0955	0.2012	0.1409
	$e_3(t)$	0.0209	0.0550	5.7288
$ITSE = \int_0^{Ts} \mathbf{e}^T(t)\mathbf{e}(t)\, t\, dt$	$e_1(t)$	0.0122	0.0540	0.0342
	$e_2(t)$	0.0071	0.0366	0.0148
	$e_3(t)$	0.0013	0.0105	67.800

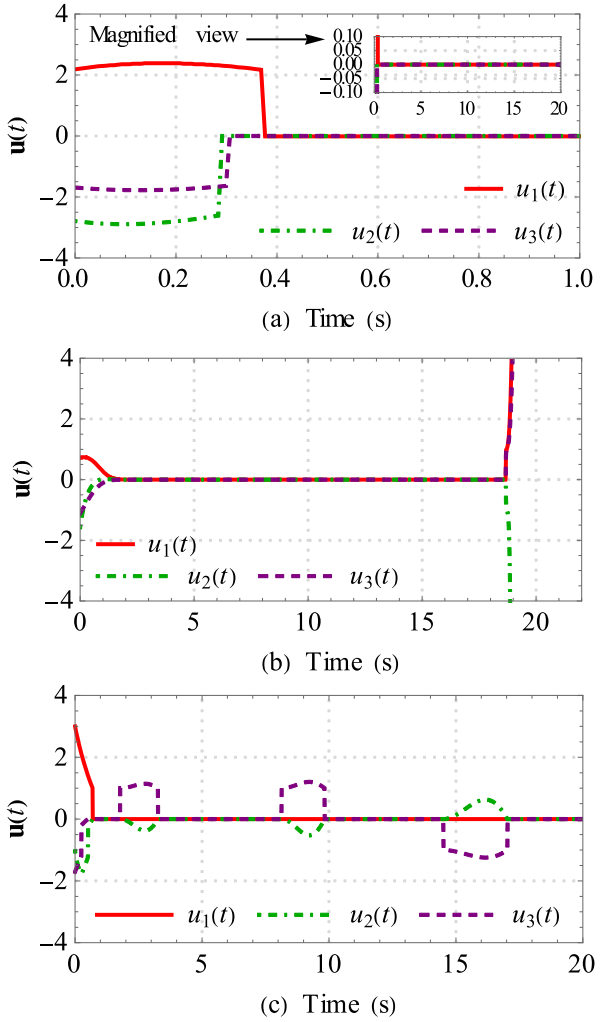

FIGURE 14. Scenario 1: Transient behaviour of the (a) RDASCS signals (14), (b) adaptive control signals (21), and (c) SMC signals (23).

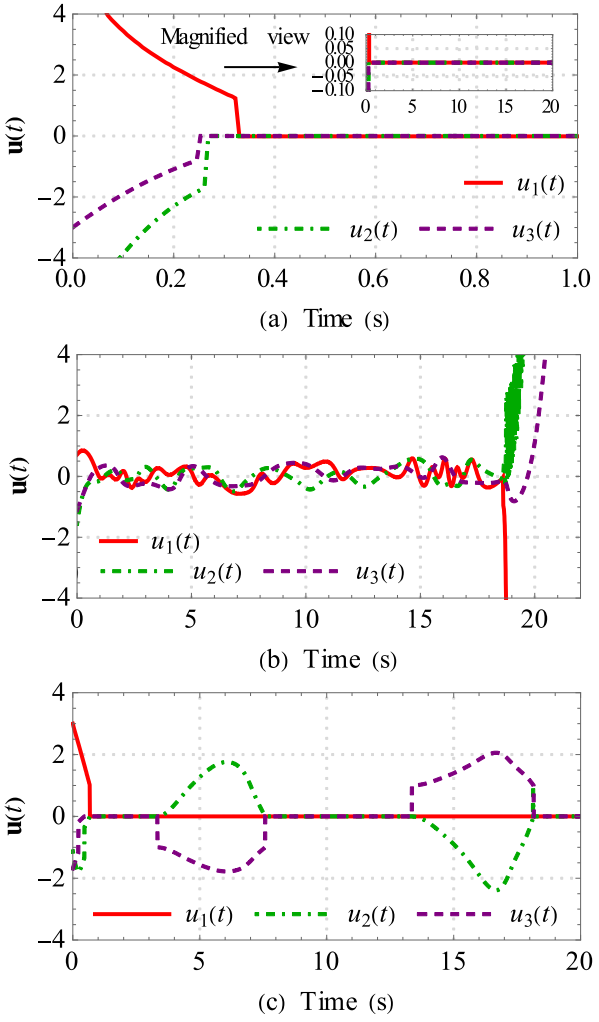

FIGURE 15. Scenario 2: Transient behaviour of the (a) RDASCS signals (14), (b) adaptive control signals (21), and (c) SMC signals (23).

by ACT (21), and by the SMC strategy (23) for 0.35 seconds and 1 second, alternatively. Simulation results in Figure 17(a) show that the proposed controller (14) brings the system synchronization error energy to zero steady-state in less than 0.4 seconds. Fig. 17(b) illustrates that controller (21) takes 0.7 seconds and controller (23) takes 0.9 seconds. This characteristic of the designed controller (14) enhances the accuracy, shows robustness and improves the stability of the closed-loop dynamical system.

The following table shows energy functions and their dissipation rate for comparison.

Table 6 is used to derive the inequality (27).

$$\left|\dot{V}_1\left(\mathbf{e}\left(t\right)\right)\right| \leq \left|\dot{V}_2\left(\mathbf{e}\left(t\right)\right)\right| \leq \left|\dot{V}\left(\mathbf{e}\left(t\right)\right)\right|. \tag{27}$$

Figure 18(a) shows the energy dissipation rate functions $\dot{V}\left(\mathbf{e}\left(t\right)\right)$ and $\dot{V}_i\left(\mathbf{e}\left(t\right)\right), i = 1, 2$ behaviour accomplished by controllers (14), (21), and (23) for 0.35 seconds and Figure 18(b) for 1 seconds. Simulation results in Figure 18(a) show that the proposed controller (14) brings the system synchronization error energy to zero steady-state in less than 0.35 seconds.

Figure 18(b) illustrates that controller (21) takes 1 second, and controller (23) takes 1.2 seconds to establish steady-state

TABLE 6. Comparison of the energy function dissipation rate.

Control input	Energy function	Derivative of the energy function
RDASCS (14)	$V\left(\mathbf{e}(t)\right)$ in (16)	$\dot{V}\left(\mathbf{e}(t)\right)$ in (20)
ACT (21)	$V_1\left(\mathbf{e}(t)\right) = \frac{1}{2}\mathbf{e}^T(t)\,\mathbf{e}(t) + \frac{1}{2}\sum_{i=1}^{3}\tilde{a}_i^2(t)$, where $\tilde{a}_i(t) = a_i - \hat{a}_i(t)$, $i = 1, 2, 3$	$\dot{V}_1\left(\mathbf{e}(t)\right) = -\mathbf{e}^T(t)\boldsymbol{\alpha}\mathbf{e}(t) - \frac{\mathbf{e}^T(t)k_1\mathbf{e}(t)}{l(\lvert\mathbf{e}(t)\rvert + k_2 e^{-k_3 t})}$
SMC strategy (23)	$V_2\left(\mathbf{e}(t)\right) = \frac{1}{2}\sum_{i=1}^{3} c_i^2 e_i^2(t)$, $c_i \in R^+$	$\dot{V}_2\left(\mathbf{e}(t)\right) = \sum_{i=1}^{3} -\alpha_{ii}c_i^2 e_i^2(t) - \gamma_{ii}\lvert c_i e_i(t)\rvert$, $c_i \in R^+$

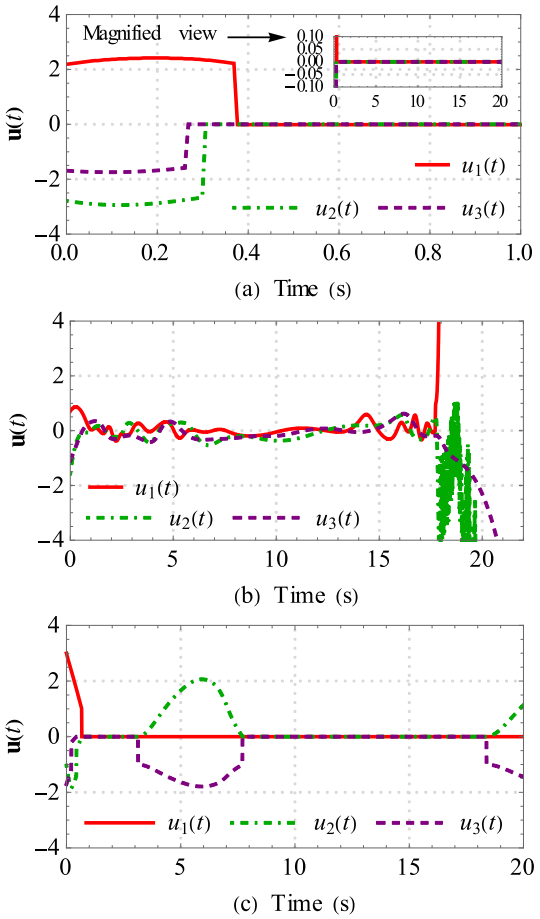

FIGURE 16. Scenario 3: Transient behaviour of the (a) RDASCS signals (14), (b) adaptive control signals (21), and (c) SMC signals (23).

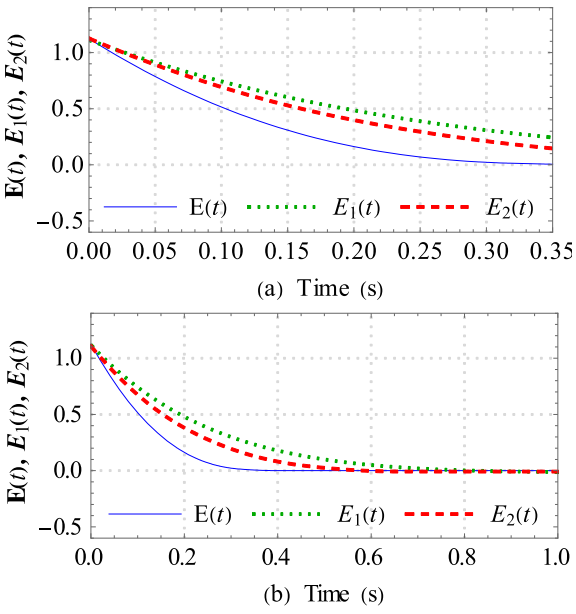

FIGURE 17. (a-b) Comparison of $\mathbf{E}(t)$, $\mathbf{E_1}(t)$, and $\mathbf{E_2}(t)$.

synchronization error energy to zero. The time gradient of constant synchronization error energy is zero. $\dot{V}(\mathbf{e}(t)) = 0$ before 0.35 seconds, $\dot{V}_1(\mathbf{e}(t)) = 0$ after 1 second, and $\dot{V}_2(\mathbf{e}(t)) = 0$ after 1.2 seconds indicate the proposed closed-loop convergence to zero faster than the other two. This attribute of the proposed method is instrumental in reducing closed-loop signal oscillations.

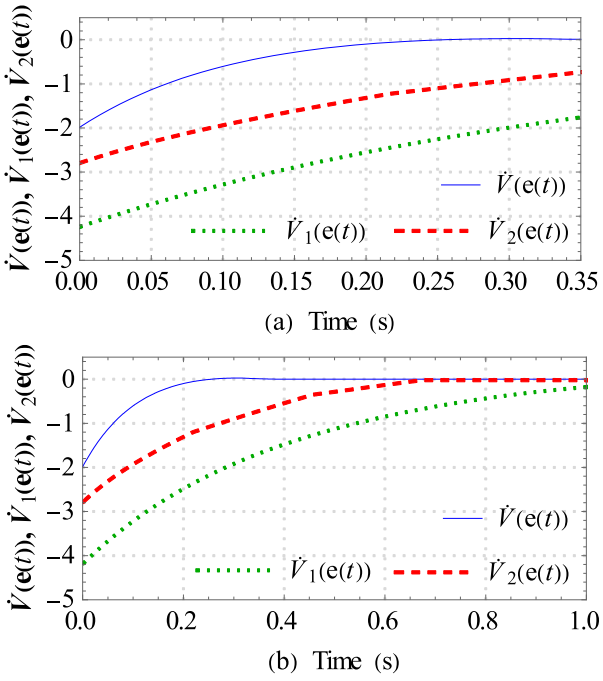

FIGURE 18. (a-b) Comparison of $\dot{V}(\mathbf{e}(t))$, $\dot{V}_1(\mathbf{e}(t))$, and $\dot{V}_2(\mathbf{e}(t))$.

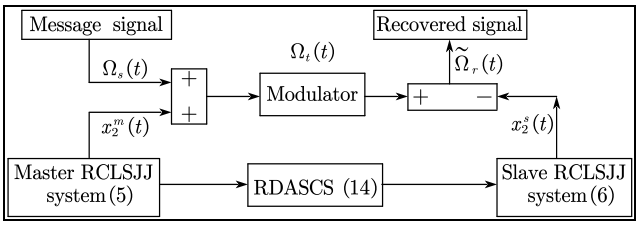

FIGURE 19. The schematic diagram for secure communications based on the MSS scheme (5-6).

The following subsection discusses applications of the proposed algorithm for the encryption/decryption of messages in secure communication systems (SCS).

C. APPLICATIONS TO SECURE COMMUNICATIONS SYSTEMS AND IMAGE ENCRYPTION AND DECRYPTION

The encryption and decryption process is a typical chaos synchronization application in secure communication systems (SCS) [44]. An encrypted signal is transmitted and decrypted at the receiving node in SCS. The decryption of the received signal is a synchronization problem, i.e. matching the received signal with the initially transmitted signal before encryption [45]. This subsection discusses two applications of the proposed method to encrypt and decrypt messages (i) One-dimensional signals and (ii) Two-dimensional signals (images). The master RCLSJJ chaotic system (5) encrypts

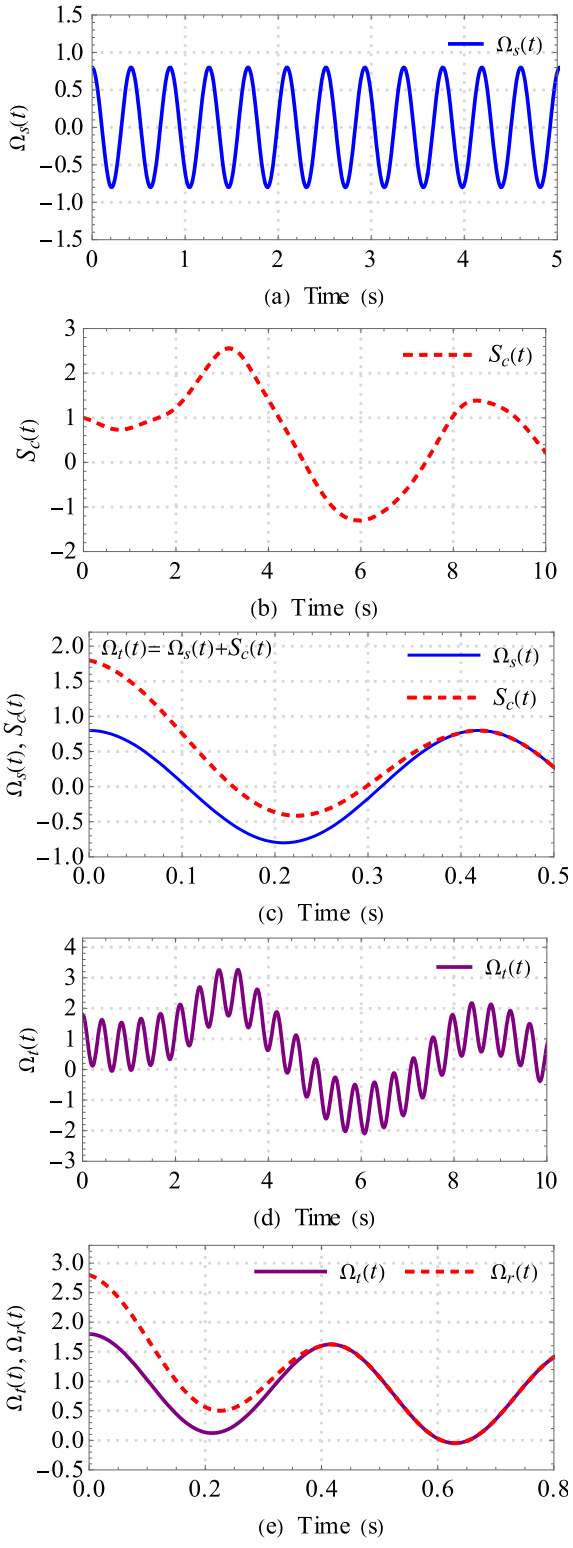

FIGURE 20. (a) Original message signal $\Omega_s(t)$, (b) chaotic carrier signal $S_c(t)$, (c) encrypted information signal $\Omega_s(t)$ and $S_c(t)$, (d) combined effect of $\Omega_s(t)$ and $S_c(t)$, where $\Omega_t(t) = \Omega_s(t) + S_c(t)$, and (e) encrypted transmitted signal $\Omega_t(t)$ and recovered signal $\Omega_r(t)$.

the message at the transmission node, and the synchronization process of the slave RCLSJJ chaotic system (6) at the receiving node decrypts the encrypted message.

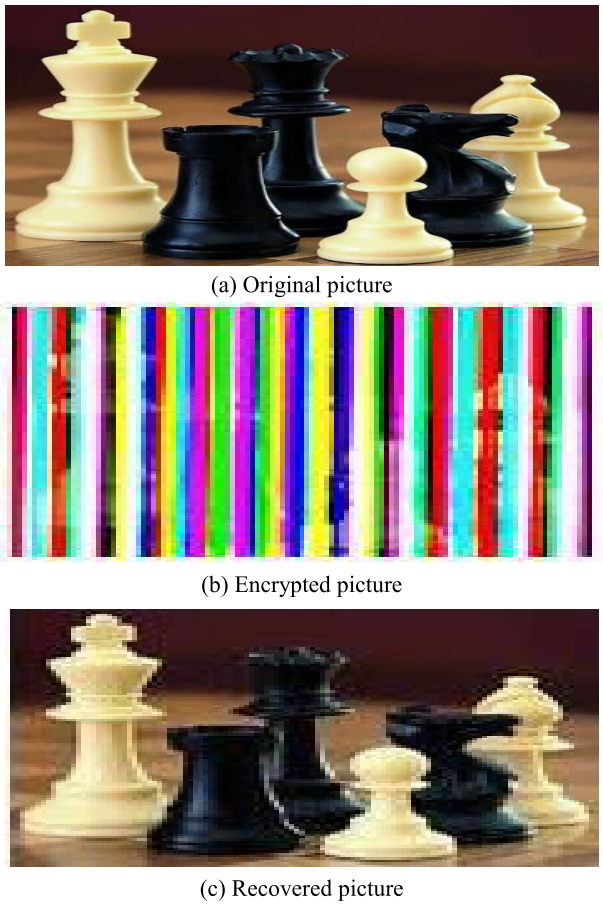

FIGURE 21. Image encryption and decryption.

Figure 19 shows a schematic diagram for the encryption and decryption scheme based on the MSS arrangement (5-6).

1) ONE-DIMENSIONAL SIGNALS

Consider a chaotic signal $\Omega_t(t) = f(S_c(t), \Omega_s(t)) = S_c(t) + \Omega_s(t) = x_2^m(t) + 0.8\cos 15t$ where $S_c(t) = x_2^m(t)$ is the chaotic carrier signal and $\Omega_s(t) = 0.8\cos 15t$ is the message signal. $x_2^s(t)$ is a signal used for the decryption of the received encrypted message. The received encrypted signal $\Omega_r(t)$ is an altered form of the $\Omega_t(t)$ due to communication channel ramifications effects, where $\Omega_r(t)$ is a signal that receives the decrypted message. In the system, these effects are considered unknown exogenous disturbances. Synchronization of $x_2^s(t)$ to $x_2^m(t)$ i.e. $x_2^s(t) - x_2^m(t) \to 0$ assures $\Omega_r(t) - \Omega_t(t) \to 0$.

Figs. 20(a-b) show the behaviour of the original message signal and chaotic carrier signal, respectively. Figures 20(c-d) depict the information signal, and Figure 20(e) demonstrates the receiver's decrypted and original signals when the slave RCLSJJ chaotic system (6) realizes synchronization with the master RCLSJJ chaotic system (5).

2) TWO-DIMENSIONAL SIGNALS (IMAGES)

Figure 21(a) shows that the original picture encryption of this picture produces an image displayed in Figure 21(b). The

encryption algorithm uses the master RCLSJJ chaotic system (5) applied to the original image. The image is decrypted using the proposed closed-loop synchronization methodology to recover the original image shown in Figure 21(c).

VII. CONCLUSION

This paper proposes a novel synchronization control technique for the master-slave unknown RCL Shunted-Josephson Junction chaotic system externally exposed to time-varying disturbances. It proves the closed-loop stability, analyzes the state-variable error using mathematical analysis, and verifies the theoretical findings using computer simulation results. These results show that the proposed adaptive controller achieves faster and smoother synchronization error convergence, and the control signals are less oscillatory. The Lyapunov second stability theorem guarantees the closed-loop's robust performance against unknown model uncertainties and exogenous disturbances. The proposed algorithm is applied to one-dimensional and two-dimensional signals in secure communication systems. Simulation results confirm that the encrypted signals are successfully decrypted at the receiver end, recovering the original signals even after exposure to disturbances in the transmission channel.

DECLARATIONS OF INTEREST

The authors declare no conflict of interest.

REFERENCES

[1] S. Otte, S. Berg, S. Luther, and U. Parlitz, "Bifurcations, chaos, and sensitivity to parameter variations in the Sato cardiac cell model," *Commun. Nonlinear Sci. Numer. Simul.*, vol. 37, pp. 265–281, Aug. 2016.

[2] A. O. A. Alamodi, K. Sun, and Y. Peng, "Chaotic attractor with varied parameters," *Eur. Phys. J. Special Topics*, vol. 229, nos. 6–7, pp. 1095–1108, Mar. 2020.

[3] N. Lahav, I. Sendiña-Nadal, C. Hens, B. Ksherim, B. Barzel, R. Cohen, and S. Boccaletti, "Topological synchronization of chaotic systems," *Sci. Rep.*, vol. 12, no. 1, p. 2508, Feb. 2022.

[4] M. Tabasi and S. Balochian, "Active fault-tolerant synchronisation of fractional-order chaotic gyroscope system," *J. Control Decis.*, vol. 8, no. 2, pp. 213–221, Jan. 2020.

[5] A. E. Motter, S. A. Myers, M. Anghel, and T. Nishikawa, "Spontaneous synchrony in power-grid networks," *Nature Phys.*, vol. 9, no. 3, pp. 191–197, Feb. 2013.

[6] U. E. Kocamaz and Y. Uyaroğlu, "Non-identical synchronization, anti-synchronization and control of single-machine infinite-bus power system via active control," *Inf. Technol. Control*, vol. 43, no. 2, pp. 166–174, Jun. 2014.

[7] S. Harshavarthini, R. Sakthivel, and F. Kong, "Finite-time synchronization of chaotic coronary artery system with input time-varying delay," *Chaos, Solitons Fractals*, vol. 134, May 2020, Art. no. 109683.

[8] F. Radicchi and H. M. Ortmanns, "Entrainment of randomly coupled oscillator networks by a pacemaker," *Phys. Rev. E, Stat. Phys. Plasmas Fluids Relat. Interdiscip. Top.*, vol. 73, pp. 1–8, Apr. 2006.

[9] X. Wang, J. Liu, H. Peng, L. Gao, J. Fottner, and P. Liu, "Input-constrained chaos synchronization of horizontal platform systems via a model predictive controller," *Proc. Inst. Mech. Eng. C, J. Mech. Eng. Sci.*, vol. 235, no. 20, pp. 4862–4872, Dec. 2020.

[10] M. Shahzad, "Internal synchronization using adaptive sliding mode," *Int. J. Robust Nonlinear Cont.*, vol. 33, no. 3, pp. 2320–2335, 2023.

[11] J. Luo, S. Qu, Y. Chen, X. Chen, and Z. Xiong, "Synchronization, circuit and secure communication implementation of a memristor-based hyper-chaotic system using single input controller," *Chin. J. Phys.*, vol. 71, pp. 403–417, Jun. 2021.

[12] Y. Huang and H. Bao, "Master-slave synchronization of complex-valued delayed chaotic Lur'e systems with sampled-data control," *Appl. Math. Comput.*, vol. 379, Aug. 2020, Art. no. 125261.

[13] I. Ahmad and M. Shafiq, "Oscillation free robust adaptive synchronization of chaotic systems with parametric uncertainties," *Trans. Inst. Meas. Control*, vol. 42, no. 11, pp. 1977–1996, Feb. 2020.

[14] J. Wang, T. Ru, J. Xia, Y. Wei, and Z. Wang, "Finite-time synchronization for complex dynamic networks with semi-Markov switching topologies: An H∞ event-triggered control scheme," *Appl. Math. Comput.*, vol. 356, pp. 235–251, Sep. 2019.

[15] M. Cuzminschi and A. Zubarev, "Chaotic behavior of a stack of intrinsic Josephson junctions at the transition to branching for overcritical currents," *Chin. J. Phys.*, vol. 71, pp. 634–642, Jun. 2021.

[16] C. B. Whan and C. L. Lobb, "Complex dynamic behaviors in RLC-shunted Josephson tunnel junction," *Phys. Rev. E, Stat. Phys. Plasmas Fluids Relat. Interdiscip. Top.*, vol. 53, pp. 405–413, Jan. 1996.

[17] A. E. Botha, Y. M. Shukrinov, and J. Tekić, "Chaos along the rc-branch of *RLC*-shunted intrinsic Josephson junctions," *Chaos, Solitons Fractals*, vol. 156, Mar. 2022, Art. no. 111865.

[18] J. Ma, P. Zhou, B. Ahmad, G. Ren, and C. Wang, "Chaos and multi-scroll attractors in RCL-shunted junction coupled Jerk circuit connected by memristor," *PLoS ONE*, vol. 13, no. 1, pp. 1–21, Jan. 2017.

[19] U. Yilmaz, S. Razmkhah, R. Collot, J. Kunert, R. Stolz, and P. Febvre, "Study of microwave resonances induced by bias lines of shunted Josephson junctions," *IEEE Trans. Appl. Supercond.*, vol. 30, no. 7, Oct. 2020, Art. no. 1301905.

[20] Y. M. Shukrinov, A. S. Abouhaswa, and A. E. Botha, "Double and triple resonance behaviour in large systems of LC-shunted intrinsic Josephson junctions," *Phys. Lett. A*, vol. 387, Jan. 2021, Art. no. 127025.

[21] E. M. Shahverdiev, "Modulated time delays, synchronized Josephson junctions in high-temperature superconductors and chaotic terahertz waves," *J. Supercond. Novel Magnetism*, vol. 34, no. 4, pp. 1125–1132, Feb. 2021.

[22] T. Noh, A. Kindseth, and V. Chandrasekhar, "Nonlocal superconducting quantum interference device," *Phys. Rev. B, Condens. Matter*, vol. 104, no. 6, Aug. 2021, Art. no. 064503.

[23] H. Vora, R. L. Kautz, S. W. Nam, and J. Aumentado, "Modeling bloch oscillations in nanoscale Josephson junctions," *Phys. Rev. B, Condens. Matter*, vol. 96, no. 5, Aug. 2017, Art. no. 054505.

[24] C. Lu, A. Liu, M. Ling, and E. Dong, "Synchronization of chaos in RCL-shunted Josephson junctions array," in *Proc. Chin. Autom. Congr. (CAC)*, Wuhan, China, Nov. 2015, pp. 1956–1961.

[25] A. E. Botha, I. R. Rahmonov, and Y. M. Shukrinov, "Spontaneous and controlled chaos synchronization in intrinsic Josephson junctions," *IEEE Trans. Appl. Supercond.*, vol. 28, no. 7, pp. 1–6, Oct. 2018.

[26] K. Benkouider, S. Vaidyanathan, A. Sambas, E. Tlelo-Cuautle, A. A. A. El-Latif, B. Abd-El-Atty, C. F. Bermudez-Marquez, I. M. Sulaiman, A. M. Awwal, and P. Kumam, "A new 5-D multistable hyperchaotic system with three positive Lyapunov exponents: Bifurcation analysis, circuit design, FPGA realization and image encryption," *IEEE Access*, vol. 10, pp. 90111–90132, 2022.

[27] A. Uçar, K. E. Lonngren, and E.-W. Bai, "Chaos synchronization in RCL-shunted Josephson junction via active control," *Chaos, Solitons Fractals*, vol. 31, no. 1, pp. 105–111, Jan. 2007.

[28] U. E. Vincent, A. Ucar, J. A. Laoye, and S. O. Kareem, "Control and synchronization of chaos in RCL-shunted Josephson junction using backstepping design," *Phys. C, Supercond.*, vol. 468, no. 5, pp. 374–382, Mar. 2008.

[29] D.-Y. Chen, W.-L. Zhao, X.-Y. Ma, and R.-F. Zhang, "Control and synchronization of chaos in RCL-shunted Josephson junction with noise disturbance using only one controller term," *Abstract Appl. Anal.*, vol. 2012, Jul. 2012, Art. no. 378457.

[30] N. Fang and J. Fang, "Generalized synchronization of chaos in RCL-shunted Josephson junction with uncertain parameters," *Appl. Mech. Mater.*, vols. 157–158, pp. 752–756, Feb. 2012.

[31] K. S. Ojo, A. N. Njah, and O. I. Olusola, "Generalized compound synchronization of chaos in different orders chaotic Josephson junctions," *Int. J. Dyn. Control*, vol. 4, no. 1, pp. 31–39, Aug. 2014.

[32] A. Khooshehmehri, S. Nasrollahi, and M. Aliyari, "Chaos synchronization in Josephson junction using nonlinear robust adaptive controller: HIL implementation," *Int. J. Dyn. Control*, vol. 10, no. 4, pp. 1228–1239, Oct. 2021.
[33] S. K. Dana, P. K. Roy, G. C. Sethia, A. Sen, and D. C. Sengupta, "Taming of chaos and synchronisation in RCL-shunted Josephson junctions by external forcing," *IEE Proc., Circuits Devices Syst.*, vol. 153, no. 5, pp. 453–460, Oct. 2006.
[34] H. K. Khalil, *Nonlinear Systems*, 2nd ed. Upper Saddle River, NJ, USA: Prentice-Hall, 2002.
[35] A. Khan and S. Kumar, "Measuring chaos and synchronization of chaotic satellite systems using sliding mode control," *Optim. Control Appl. Methods*, vol. 39, no. 5, pp. 1597–1609, May 2018.
[36] M. P. Aghababa and H. P. Aghababa, "Chaos synchronization of gyroscopes using an adaptive robust finite-time controller," *J. Mech. Sci. Technol.*, vol. 27, no. 3, pp. 909–916, Mar. 2013.
[37] Z. Rashidnejad and P. Karimaghaee, "Synchronization of a class of uncertain chaotic systems utilizing a new finite-time fractional adaptive sliding mode control," *Chaos, Solitons Fractals X*, vol. 5, Mar. 2020, Art. no. 100042.
[38] J. Matkowski, "A mean-value theorem and its applications," *J. Math. Anal. Appl.*, vol. 373, no. 1, pp. 227–234, Jan. 2011.
[39] M. Jiang, J. Luo, D. Jiang, J. Xiong, H. Song, and J. Shen, "A cuckoo search-support vector machine model for predicting dynamic measurement errors of sensors," *IEEE Access*, vol. 4, pp. 5030–5037, 2016.
[40] A. Dianov, "Recommendations and typical errors in design of power converter PCBs with shunt sensors," *IEEE Open J. Ind. Electron. Soc.*, vol. 3, pp. 329–338, 2022.
[41] M. Luo, R. Wang, S. Guo, J. Wang, J. Zou, and R. Huang, "Impacts of random telegraph noise (RTN) on digital circuits," *IEEE Trans. Electron Devices*, vol. 62, no. 6, pp. 1725–1732, Jun. 2015.
[42] R. L. Burden, J. D. Fairs, and A. M. Burden, *Numerical Analysis*, 10th ed. Boston, MA, USA: CENAGE Learning, 2014.
[43] S. M. Shinners, *Modern Control System Theory and Design*. New York, NY, USA: Wiley, 1998.
[44] C. Zhou, C. Wang, W. Yao, and H. Lin, "Observer-based synchronization of memristive neural networks under DoS attacks and actuator saturation and its application to image encryption," *Appl. Math. Comput.*, vol. 425, Jul. 2022, Art. no. 127080.
[45] L. Wang, T. Dong, and M.-F. Ge, "Finite-time synchronization of memristor chaotic systems and its application in image encryption," *Appl. Math. Comput.*, vol. 347, pp. 293–305, Apr. 2019.

MUHAMMAD SHAFIQ (Senior Member, IEEE) received the Ph.D. degree from Chiba University, Japan, in 1997. He works as an Associate Professor with the Department of Electrical and Computer Engineering, Sultan Qaboos University, Muscat, Oman. Before this position, he spent over 20 years working in various government and semi-government institutions, including as a Professor of automation and control at the Ghulam Ishaque Khan Institute of Engineering, Sciences and Technology, Pakistan, and as a Faculty Member at the Systems Engineering Department, King Fahad University for Petroleum and Minerals, Saudi Arabia. He is among the authors of more than 120 journals and conference papers and several book chapters. His research interests include control systems, machine learning and artificial intelligence, neuro control, adaptive control, robotics, mechatronics, cybersystems, chaos control, and synchronization. He chaired several conference sessions.

ISRAR AHMAD received the Ph.D. degree from Northern University Utara Malaysia, in 2017. He works with the College of Applied Sciences, University of Technology and Applied Sciences Nizwa, Ministry of Higher Education, Oman. He is among the authors of more than 36 journals and conference papers. His research interests include chaos synchronization and control of chaotic systems. He is an editorial board member in different esteemed journals.

BASHIR NADERI received the Ph.D. degree in applied mathematics from Pyame Noor University (PNU), Iran, in 2016. He is currently an Assistant Professor of mathematics at PNU. His research interests include dynamical systems, optimal control, chaotic systems, and secure communications.